

Fusing Optical and SAR time series for LAI gap filling with multioutput Gaussian processes ¹

Luca Pipia^{a,*}, Jordi Muñoz-Mari^a, Eatidal Amin^a, Santiago Belda^a, Gustau Camps-Valls^a,
Jochem Verrelst^a

^a*Image Processing Laboratory (IPL), Parc Científic, Universitat de València, 46980 Paterna, València, Spain.*

Abstract

The availability of satellite optical information is often hampered by the natural presence of clouds, which can be problematic for many applications. Persistent clouds over agricultural fields can mask key stages of crop growth, leading to unreliable yield predictions. Synthetic Aperture Radar (SAR) provides all-weather imagery which can potentially overcome this limitation, but given its high and distinct sensitivity to different surface properties, the fusion of SAR and optical data still remains an open challenge. In this work, we propose the use of Multi-Output Gaussian Process (MOGP) regression, a machine learning technique that learns automatically the statistical relationships among multisensor time series, to detect vegetated areas over which the synergy between SAR-optical imageries is profitable. For this purpose, we use the Sentinel-1 Radar Vegetation Index (RVI) and Sentinel-2 Leaf Area Index (LAI) time series over a study area in north west of the Iberian peninsula. Through a physical interpretation of MOGP trained models, we show its ability to provide estimations of LAI even over cloudy periods using the information shared with RVI, which guarantees the solution keeps always tied to real measurements. Results demonstrate the advantage of MOGP especially for long data gaps, where optical-based methods notoriously fail. The leave-one-image-out assessment technique applied to the whole vegetation cover shows MOGP predictions improve standard GP estimations over short-time gaps (R^2 of 74% vs 68%, RMSE of 0.4 vs 0.44 [m^2m^{-2}]) and especially over long-time gaps (R^2 of 33% vs 12%, RMSE of 0.5 vs 1.09 [m^2m^{-2}]). A second assessment is focused on crop-specific regions, clustering pixels fulfilling specific model

*Corresponding author

¹Tel: +34-96-354-40-67; Fax: +34-96-354-32-61.

¹Paper published at Remote Sensing of Environment Volume 235, 15 December 2019, 111452, doi: <https://doi.org/10.1016/j.rse.2019.111452>

conditions where the synergy is profitable. Results reveal the MOGP performance is crop type and crop stage dependent. For long time gaps, best R^2 are obtained over maize, ranging from 0.1 (tillering) to 0.36 (development) up to 0.81 (maturity); for moderate time gap, $R^2 = 0.93$ (maturity) is obtained. Crops such as wheat, oats, rye and barley, can profit from the LAI-RVI synergy, with R^2 varying between 0.4 and 0.6. For beet or potatoes, MOGP provides poorer results, but alternative descriptors to RVI should be tested for these specific crops in the future before discarding synergy real benefits. In conclusion, active-passive sensor fusion with MOGP represents a novel and promising approach to cope with crop monitoring over cloud-dominated areas.

Keywords: Data Time Series, Gaussian Process Regression (GPR), Machine Learning, Sentinel-2, Sentinel-1, synergy, Cloud-induced data gaps, leaf area index (LAI), Radar Vegetation Index (RVI)

1. Introduction

Monitoring the dynamics of Earth's surface properties constitutes the ultimate purpose of remote sensing. Among the objectives of the multiple Earth observation (EO) missions launched in the last decades, primary importance has been given to natural and managed vegetation land covers (Chevrel et al., 1981; Huete et al., 2002; Zhang et al., 2003; Boles et al., 2004; Dierckx et al., 2014). The strong relationship between the response of vegetation in the visible and near-infrared spectrum and its biophysical activities led the preference towards optical satellite sensors, even if on average clouds prevent measuring more than 70% of Earth surface at any time over the globe (Chelton and Wentz, 2005). Besides, only to some extent the revisit time was considered a demanding constraint for these satellite missions, since its increase goes at the expense of the imagery's spatial resolution. This trade-off narrowed down the analysis to global vegetation dynamics, with limitations over areas with persistent cloud covers.

A major breakthrough was achieved with the Sentinel space missions of the Copernicus Space programme (Berger et al., 2012). Covering a range of technologies, such as radar and multispectral imaging instruments, each mission comprises a constellation of two satellites, thereby allowing land, ocean and atmospheric monitoring with an unprecedented spatial-time-spectral sampling (Malenovský et al., 2012). With the Sentinel2A/B (S2) sensors, launched

in June 2015 and April 2017 respectively, multispectral images have become freely available with a maximum revisit of 5 days (Drusch et al., 2012). New challenges in monitoring the phenological evolution of vegetation land covers are then posed. 1) The high-resolution of S2 imagery allows extending global analysis to field-scale homogeneous areas and identifying different growing stages in terms of timing as well as abundance. 2) Simple vegetation indices such as the normalized difference vegetation index (NDVI) (Tucker, 1979) or more complex descriptors such as the green leaf area index (LAI) (Jonckheere et al., 2004) can be estimated at high temporal sampling and a level of detail suitable for local studies. Nonetheless, the limitations due to the presence of clouds are reduced but not eliminated. The need for cloud-free acquisitions becomes even more critical in the case of crop monitoring, especially during the key development stages between seedling and flowering. Precise and timely delivered EO data provide farmers with the opportunity to intervene when necessary to improve crop yields or water-use efficiency (Baret et al., 2010; Duchemin et al., 2015). Yet, cloud contamination may drastically reduce the actual number of samples at disposal over a specific area of interest, thereby limiting the reliability of farming recommendations.

Multiple methods have been proposed to deal with the presence of gaps in the temporal series of EO-based optical vegetation descriptors. These methods either consider the time series as a whole (Golyandina and Osipov, 2007; Verger et al., 2013; Bacour et al., 2006), or define a moving time window for the analysis (Chen et al., 2004; Verger et al., 2011; Jonsson and Eklundh, 2002). The methods belonging to both approaches are compared in Kandasamy et al. (2013). With the aim of generating finer and timely LAI products at potentially global scale, multisensors approach using spatio-temporal enhancement methods have been also pursued. MODIS and Landsat information have been merged using canopy spectral invariants theory (Ganguly et al., 2012) and spatio-temporal adaptive models, first at reflectance level (Gao et al., 2006, 2012; Wang et al., 2014) and later using biophysical parameters such as LAI (Houborg et al., 2016) or evapotranspiration (Cammalleri et al., 2014). The main limitation all these methods share is for long data gaps (>2 months), common on regions with dominant cloudiness, vegetation changes are mostly ignored and retrievals cannot be trusted.

An alternative solution is represented by synthetic aperture radar (SAR) imagery. On the one hand, clouds are not an issue for these sensors. On the other hand, SAR backscattering is related to observation geometry, but also to physical properties of the surface such

as soil roughness, soil moisture and, particularly interesting in this context, vegetation cover (Ulaby et al., 1981; Ferrazzoli et al., 1992). The presence of vegetation generates the so-called volumetric scattering, which causes the redistribution of energy in the cross-polar band and evinces the sensitivity of SAR response to vegetation thickness (Bousbih et al., 2017). In case of crop monitoring, the backscattering from the ground dominates the crop’s early and late phenological stages but the vegetation contribution becomes higher in between (Mattia et al., 2003; Cloude, 2010). Thus, SAR sensors represent a suitable solution to create gap-free data collections for continuous vegetation mapping. Several studies exist on the description of crop phenology evolution with SAR imagery alone (Bousbih et al., 2017), using both single-pol (Satalino et al., 2014) and full-pol (Wiseman et al., 2014; Lopez-Sanchez et al., 2013) information. The sensitivity of SAR backscattering to vegetation growth also led to the definition of a Radar Vegetation Index (RVI), when dealing with fully polarimetric data (Kim and van Zyl, 2009; Kim et al., 2014; Veloso et al., 2017), and a simplified version of it when only dual-pol data are available (Kim and van Zyl, 2001). In general, SAR co-polar and cross-polar combinations are more related to optical vegetation descriptors as NDVI and LAI than single bands (Kim et al., 2012; Fieuzal et al., 2013), but the degree of this relationship is crop- as well as wavelength-dependent (Veloso et al., 2017). Additionally, shorter wavelengths, such as C-($\sim 5\text{cm}$) or X ($\sim 3\text{cm}$) bands, are more sensitive to vegetation small-scale properties than L-band ($\sim 23\text{cm}$), and their interaction with the soil may be dominant in case of sparse vegetation layers such as croplands in early stages (Ulaby et al., 1981). From this point of view, the Sentinel1A/B (S1) sensors, launched in April 2014 and 2016 respectively, are suited for monitoring croplands: they provide SAR images at C-band of all over the world with a maximum revisit time of 6 days (Torres et al., 2012). Successful use of S1 collections include crop classification (Torbick et al., 2017; Xu et al., 2019) and monitoring (via classification of different vegetative stages (Mandal et al., 2018)) but, due to SAR sensitivity to many surface parameters, these approaches are not yet robust enough for operational monitoring services or crop yield estimation. At present, filling the temporal gaps of optical data over vegetation-covered surfaces with SAR observations is still an open challenge that requires finding a proper way to exploit their synergy: these two data modalities contain both complementary as well as common information that should be disentangled for their synergistic exploitation.

In the last years, several efforts have been devoted to blend radar and optical information.

Many applications benefit from the fused information, including building structure detection (Tupin and Roux, 2003), urban classification (Haas and Ban, 2017), heterogeneous land cover and crop classification (Camps-Valls et al., 2008; Amarsaikhan et al., 2007; Dusseux et al., 2014), yield prediction (Baup et al., 2015), soil moisture mapping (Gao et al., 2017), LAI estimation (Dusseux et al., 2014) and environmental hazards detection (Errico et al., 2015), among others. Nonetheless, despite the variety of fusion techniques used during the years, a concrete rationale on their applicability is still missing (Joshi et al., 2016). First results on the generation of synthetic RGB images using deep neural network (NN) architectures trained on S1 and S2 collections have been recently presented in He and Yokoya (2018); Schmitt et al. (2018), yet their performances are still insufficient for any operational purpose. The complementarity of active and passive data for NDVI reconstruction has been shown in Scarpa et al. (2018) using convolutional NNs trained over S1-S2 short time series. They provide an assessment based on similarity of the spatial patterns but not a quantitative estimation of absolute errors at pixel level, nor a physically interpretable model of the information merging or a characterization of the estimation uncertainty. Altogether, a robust method able to merge active-passive data over vegetation and improve the quantitative retrieval from a primary source (i.e., optical) by exploiting only the amount of information shared with a secondary source (i.e., SAR) is still to be defined.

In this work, we propose a novel fusion approach for exploiting the information of S1 and S2 time series data collections at pixel level, and tackle the problem of cloud-induced data gaps over vegetated areas. We explore the use of S1-based RVI time series to fill the missing S2-based LAI information with Multi-Output Gaussian Processes (MOGPs). MOGP is a powerful statistical method able to capture the dependencies among any kind of multiple, yet related, data collections (Alvarez et al., 2012). The use of this technique for remote sensing applications is absolutely new. To the best of our knowledge, only a simplified version of MOGP has been used to provide gap-free soil moisture time series by merging multi-frequency soil moisture products (Piles et al., 2018). The approach pursued here is more challenging because it investigates the potentials of MOGP to learn the relationship between two totally different sensors, build a cross-domain kernel function able to transfer information across the time series, and do predictions (and provide associated gapfilled intervals) on regions where no optical data are available. MOGP can be trained at any scale, e.g., per-pixel or averaged per

land cover. For each multisensor time series, it creates a specific model providing a prediction of the vegetation descriptors at any date along with an estimation of its uncertainty. Of interest hereby is that the parameters of each model are shown to describe directly the correlation between optical and SAR time series. As such, the MOGP method provides a quantifiable measure on how well two distinct EO products sources are expected to complement each other in time series gap filling.

After providing a theoretical background of standard GP and MOGP (Section 2), LAI and RVI collections over a study area in north west of Iberian peninsula (Section 3) are used to illustrate the proposed MOGP and the active-passive synergy. The results (Sections 4) on LAI gap-filling over a specific crop field are presented for propaedeutic purposes. Their analysis allows presenting a clear interpretation of the key role played by MOGP model’s parameters. This order facilitates understanding the findings obtained when MOGP is extended to the spatial domain for cloud-free LAI map retrievals, and paves the path to discuss the potentials and limitations of the proposed method (Section 5).

2. Methodology

Standard Gaussian Process Regression (GP) models are state-of-the-art statistical methods for regression and function approximation. In recent years, we have successfully applied GPs for the retrieval of biophysical parameters from optical imagery, see (e.g. Verrelst et al., 2012, 2013b,a; Campos-Taberner et al., 2016; Amin et al., 2018; Verrelst et al., 2015; Camps-Valls et al., 2015, 2016, 2019). GP models yield not only predictions of the phenomenon to be characterized by means of a non-parametric modelling, but also an estimation of their uncertainty. A general introduction to GP can be found in Rasmussen and Williams (2006); Camps-Valls et al. (2016). In the following we briefly review the standard GP and MOGP formulations, adapted to the general needs of this study.

2.1. GP modeling of single output variable

Let $\mathcal{D} = \{t_i, y_i\}_{i=1}^N$ be a set of N pairs of a generic parameter y_i extracted from data acquired at times t_i . We use these pairs to learn a function f able to predict the parameter estimates at new times. Instead of assuming a parametric form for f , we start by assuming

an additive noise model:

$$y_i = f(t_i) + e_i, \quad e_i \sim \mathcal{N}(0, \sigma_n^2), \quad (1)$$

where $t \in \mathbb{R}$, σ_n^2 is the noise variance and $f(t)$ is the unknown (and nonparametric) latent function to be found. Defining $\mathbf{t} = [t_1, \dots, t_N]^\top$, the GP model assumes that $f(\mathbf{t})$ is a Gaussian-distributed random vector with zero-mean and covariance matrix $\mathbf{K}(\mathbf{t}, \mathbf{t})$, i.e. $f(\mathbf{t}) \sim \mathcal{N}(\mathbf{0}, \mathbf{K})$. The elements ij of the covariance matrix are calculated by means of a kernel function $k(t_i, t_j)$ encoding the similarity between input time points t_i and t_j . The square exponential (SE) or the Matern 3/2 kernel functions are often used for this purpose (Rasmussen and Williams, 2006).

The Bayesian framework allows us to estimate the distribution of f_* at the test point t_* conditioned on the training data, $p(f_* | \mathcal{D}, t_*)$. According to the GP formulation, $f(t_*)$ is normally distributed with mean and variance given by:

$$\begin{aligned} f(t_*) &= \mu_{\text{GP}}(t_*) = \mathbf{k}_*^\top (\mathbf{K} + \sigma_n^2 \mathbf{I}_N)^{-1} \mathbf{y} \\ \sigma_f^2(t_*) &= \sigma_{\text{GP}}^2(t_*) = c_* - \mathbf{k}_*^\top (\mathbf{K} + \sigma_n^2 \mathbf{I}_N)^{-1} \mathbf{k}_*, \end{aligned} \quad (2)$$

where $\mathbf{k}_* = [k(t_*, t_1), \dots, k(t_*, t_N)]^\top$ is an $N \times 1$ vector, $\mathbf{y} = [y_1, \dots, y_N]^\top$ and $c_* = k(t_*, t_*) + \sigma_n^2$. The model hyperparameters are obtained by maximizing the marginal likelihood of the model (Rasmussen, 2004).

2.2. GP modeling of multiple output variables

One limitation of the previous GP model formulation is that it applies only to scalar functions, i.e. we can predict only one target variable at a time. A straightforward strategy to deal with several target variables is to develop as many individual GP models as target variables. While generally good performance is attained in practice, the approach has a clear shortcoming: the obtained models are independent and do not take into account the relationships among outputs.

In order to handle this problem, we propose a Multi-output Gaussian Process (MOGP) model based on the *linear model of coregionalization* (LMC) (Alvarez et al., 2012), also known as *co-kriging* in the field of geostatistics (Journel and Huijbregts, 1978). Here, we describe the rationale of the MOGP approach; see Alvarez et al. (2012) for details of the mathematical formulation.

Being D the number of outputs of interests, i.e. the number of correlated parameters we want to link in the prediction model, each output function $f_d(t)$ can be expressed as a linear combination of groups of R_q latent functions (Journal and Huijbregts, 1978) sampled from Q independent GPs:

$$f_d(t) = \sum_{q=1}^Q \sum_{r=1}^{R_q} a_{d,q}^r u_q^r(t), \quad d = 1, \dots, D \quad (3)$$

where $a_{d,q}^r$ are scalar coefficients, and $u_q^r(\mathbf{x})$ are latent functions sampled from the GP q with zero mean and covariance \mathbf{K}_q . So as to simplify the equations that follows, we assume that all outputs have the same number of training samples, N . The formulation where each output has a different number of sources can be straightforwardly obtained.

Being $\mathbf{T}_d = [t_1^d, \dots, t_N^d]^\top$ the vector containing the time samples of the output d and $\mathbf{T} = [\mathbf{T}_1^\top, \dots, \mathbf{T}_D^\top]^\top$ the one containing all of them, it can be shown (Alvarez et al., 2012) that the full covariance (matrix) of the LMC model can be expressed as:

$$\mathcal{K}(\mathbf{T}, \mathbf{T}) = \sum_{q=1}^Q \mathbf{B}_q \otimes \mathbf{K}_q(\mathbf{T}, \mathbf{T}), \quad (4)$$

where \otimes is the Kronecker product and $\mathbf{B}_q \in \mathbb{R}^{D \times D}$ are rank- R_q positive definite matrices known as *coregionalization* matrices. These matrices are the real core of the method because they encode the relationships among the multiple outputs.

Rearranging the scalar coefficients of each output q in (3) as $\mathbf{a}_q^i = [a_{1,q}^i, \dots, a_{D,q}^i]^\top$ with $i = 1, \dots, R_q$, and stacking them in the matrix $\mathbf{A}_q = [\mathbf{a}_q^1, \dots, \mathbf{a}_q^{R_q}]$, each *coregionalization* matrix is related to the coefficients of LMC model as follows:

$$\mathbf{B}_q = \mathbf{A}_q \mathbf{A}_q^\top. \quad (5)$$

By grouping the output functions as $\mathbf{f}(t) = [f_1(t), \dots, f_D(t)]^\top$, the multi-output prediction and uncertainty at a new input value t_* is given by:

$$\begin{aligned} \mathbf{f}(t_*) &= \mu_{\text{MOGP}}(t_*) = \mathcal{K}_{t_*}^\top (\mathcal{K}(\mathbf{T}, \mathbf{T}) + \Sigma \otimes \mathbf{I}_N)^{-1} \bar{\mathbf{y}}, \\ \sigma_f^2(t_*) &= \sigma_{\text{MOGP}}^2(t_*) = \mathcal{K}_{**} - \mathcal{K}_{t_*}^\top (\mathcal{K}(\mathbf{T}, \mathbf{T}) + \Sigma \otimes \mathbf{I}_N)^{-1} \mathcal{K}_{t_*}, \end{aligned} \quad (6)$$

where $\Sigma \in \mathbb{R}^{D \times D}$ is a diagonal matrix containing the variance of the noise of each output, $\bar{\mathbf{y}}$ is the vector obtained by concatenating all the samples of the D outputs, $\mathcal{K}_{t_*} \in \mathbb{R}^{D \times ND}$ is composed by blocks $\mathbf{K}_q(t_*, \mathbf{T}_d)$ for $d = 1, \dots, D$, and $q = 1, \dots, Q$ (Alvarez et al., 2012).

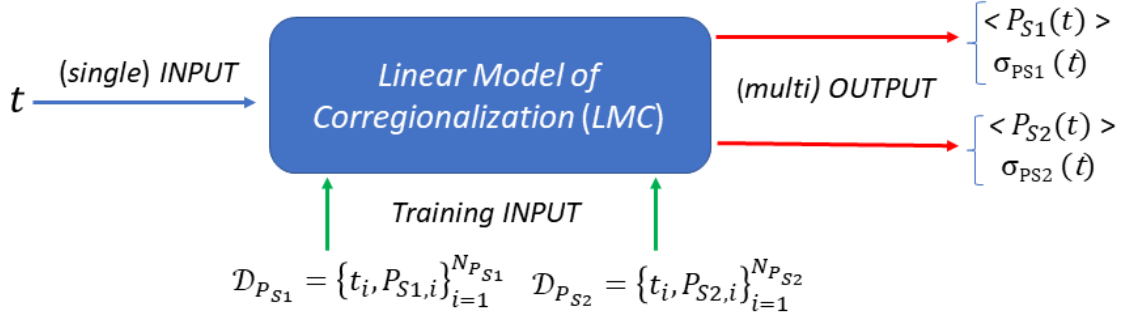


Figure 1: Sketch of MOGP modelling based on the Linear Coregionalization Model (LMC). The time series of the two input parameters to be linked by MOGP, $\mathcal{D}_{P_{S1}}$ and $\mathcal{D}_{P_{S2}}$, are used to train the model. The trained MOGP model provides a prediction of P_{S1} and P_{S2} along with their uncertainty for each input time t .

2.3. MOGP model simplification

In order to adapt MOGP formulation to model the active-passive synergy, we assume only one parameter time series is available from each imagery ($D = 2$). Referring to them as P_{S1} and P_{S2} , the collections $\mathcal{D}_{P_{S1}} = \{t_i, P_{S1,i}\}_{i=1}^{N_{P_{S1}}}$ and $\mathcal{D}_{P_{S2}} = \{t_i, P_{S2,i}\}_{i=1}^{N_{P_{S2}}}$ represent the information to be used for training purposes. Moreover, we posit that the two outputs are obtained as a linear combination of latent functions from two independent GPs ($Q = 2$) sampled only once ($R_q = 1$). This simplification, also known as *semiparametric latent factor model* (SLFM) (Alvarez et al., 2012) leads to the definition of the reference model as follows:

$$\mathbf{f}(t) = \begin{bmatrix} f_{P_{S1}}(t) \\ f_{P_{S2}}(t) \end{bmatrix} = \begin{bmatrix} a_{1,1}^1 u_1^1(t) + a_{1,2}^1 u_2^1(t) \\ a_{2,1}^1 u_1^1(t) + a_{2,2}^1 u_2^1(t) \end{bmatrix} = \mathbf{a}_1^1 u_1^1(t) + \mathbf{a}_2^1 u_2^1(t). \quad (7)$$

Accordingly, the two *coregionalization* matrices are rank-1 and related to the model's coefficients as:

$$[B_1] = \mathbf{a}_1^1 \mathbf{a}_1^{1T} \quad [B_2] = \mathbf{a}_2^1 \mathbf{a}_2^{1T}. \quad (8)$$

The expressions in (7) and (8) constitute the basic structure of the multi-output model used for our analysis. On the one hand, the two independent GPs will be able to account for details of the two time series with a magnitude and at a time scale defined by the hyperparameters of each \mathbf{K}_q after the training step. On the other hand, whether or not these details are shared between the two outputs along time will be determined by the components of \mathbf{a}_1 and \mathbf{a}_2 . Note that the ideal case is a trained model with a dominant GP with all-ones vector \mathbf{a} , i.e.

completely shared by the two outputs, and a second possibly negligible GP with a null-vector \mathbf{a} . This corresponds to the case of two perfectly correlated parameters P_{S1} and P_{S2} . Finally, it is worth stressing that the only input to the trained MOGP model is the time t at which the parameters must be estimated, as described visually in the sketch of Figure 1.

2.4. Model set-up and training

For the implementation of the MOGP, we use the GPy python library freely distributed by the ML Group of the Sheffield University (GPy, 2012). From each stack of the two coregistered collections, $\mathcal{D}_{P_{S1}}$ and $\mathcal{D}_{P_{S2}}$, a time series is extracted at pixel level. Afterwards, the Covariance kernel is set to Matern3/2, an optimum trade-off between preserving the time variability of training information and avoiding excessive smoothing effects (Rasmussen and Williams, 2006). The maximum degrees of freedom of the model described in Section 2.3 is 10: 3 for each GP Covariance parameters (variance, lengthscale, noise) and 2 for each rank-1 matrix $[B]$. By fixing the kernel’s variance to 1, we reduce them to 8 (6 model parameters +2 noise standard deviations) and let the matrix B account directly for the data dispersion. The two collections of training samples are normalized with respect to their mean value and variance, and stacked to generate the vectors \mathbf{T} in (4) and $\bar{\mathbf{y}}$, in (6). The result is passed to GPy for the hyperparameter optimization through maximization of the marginal likelihood. Finally, the covariance matrices $k_q(\mathbf{T}, \mathbf{T})$, with $q = 1, 2$ are calculated (Alvarez et al., 2012). The computational time for the training step at pixel level increases with the total number of training samples and is proportional to the cost of inverting the expression in (6), i.e. $O(n^3)$ for GPy library (GPy, 2012). Once the MOGP model is trained, the only input it expects is time: for any value, it provides the corresponding estimation of the two outputs, \mathcal{P}_{S1} and \mathcal{P}_{S2} , along with their uncertainty. The new version of optical-based \mathcal{P}_{S2} is essentially a smoothed variant of the training input over period where samples were available, but over cloud-induced gaps the solution is obtained from SAR-based \mathcal{P}_{S1} according to the linking rule MOGP has learned during the training. The key benefit of MOGP is that the estimation of each output at t_* is always obtained by keeping into account the relationship of the two outputs.

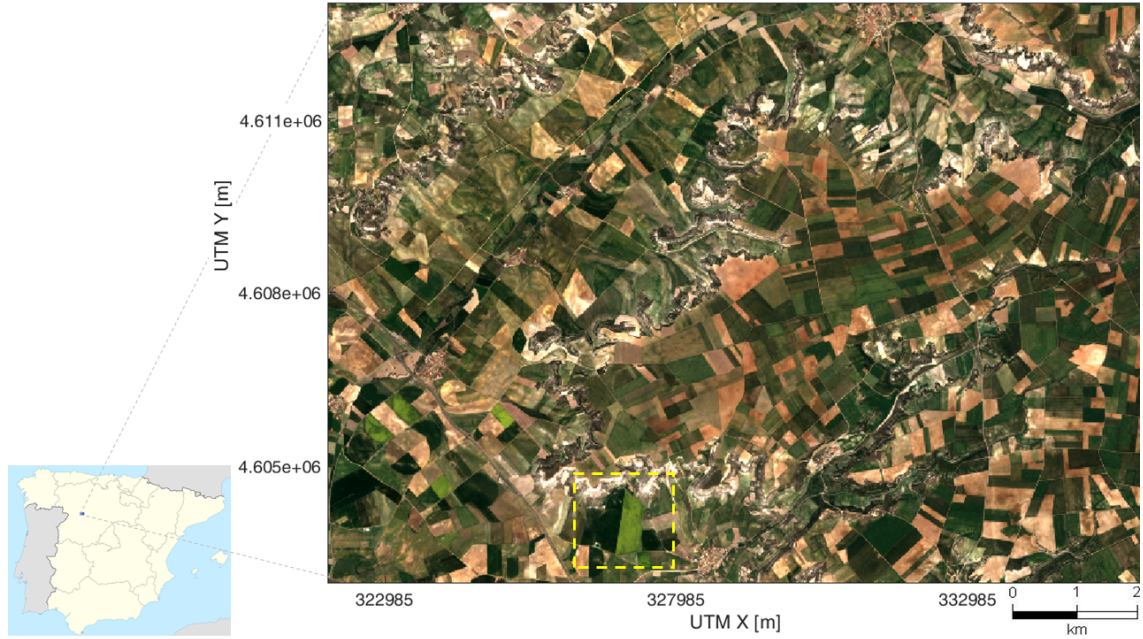


Figure 2: RGB image of the crop AOI in Castile and Leon region, Northwest Iberian peninsula, from Sentinel2 capture of 2017, April 12th. The yellow dotted rectangle delimits the subset analyzed in Section 4.2.2.

3. Study area and time series preprocessing

3.1. Study area

The Area of Interest (AOI) selected for the study is a crop region in Castile and León, in north west of the Iberian peninsula, of approximately 140 km² (Figure 2). The AOI belongs to a wider validation region of the H2020 Sensagri Project (Amin et al., 2018). A land cover map is generated yearly since 2013 using a random forest classifier, trained on in-situ data collected by the ITACYL (Gómez et al., 2018). The area selected for this work mainly corresponds to a dryland farming area with winter crops including cereals, wheat, barley and forage. A part of the arable land is also irrigated in summer with water stored in reservoirs. The main irrigated crops are maize, barley, wheat, sugar beet, alfalfa and potato.

3.2. Preprocessing of Optical time series

The collection of S2 images over the AOI was gathered from Theia datahub (Hagolle et al., 2010), where multispectral reflectance images are available at tile level. A total amount of 97 cloud-free or at least partially-cloudy S2 images were downloaded, unevenly spaced between November 2015 and October 2018. From atmospherically corrected S2 data, two

$\% \rho_s > 0.95$	2/20	3/16	4/15	5/15	6/20	7/14	8/19	9/06	10/12	11/11	12/23
VV	96.6	97.2	97.1	97.7	97.5	97.3	97.2	97.3	97.4	97.2	96.5
VH	97.1	97.6	97.0	97.2	96.4	95.8	95.5	96.4	96.1	96.7	96.8
VH/VV	96.6	97.2	97.1	97.7	97.5	97.4	97.2	97.3	97.4	97.2	96.5
RVI	97.7	98.1	98.3	98.6	98.1	97.5	97.0	97.4	97.4	97.8	97.4

Table 1: Percentage of vegetation pixels with spatial correlation $\rho_s > 0.95$ between ascending and descending daily acquisitions, throughout 2017.

collections of products were generated. 1) NDVI time series at 10 m was obtained from the S2 topography-corrected reflectance collection. 2) The standard GP regression model presented in [Amin et al. \(2018\)](#) was applied to generate green LAI time series at 10m. The model, trained with LAI in-situ measurements collected in Barrax, Spain ([Verrelst et al., 2013b](#)), during different campaigns and both real and synthetic atmospherically corrected S2 data, provided a $R^2 = 0.89$. It accepts as input the S2 bands at 10m and 20 m and generates as output the prediction of LAI at pixel level along with its uncertainty.

3.3. Preprocessing of SAR time series

The active nature of S1 imagery makes both ascendant and descendant orbits useful to monitor the AOI: orbits 74 and 154 were identified for this purpose. As no interferometric study was envisaged, radar amplitude data were downloaded from ESA’s Scientific Hub in the Ground Range Detected format. A comprehensive collection of 246 and 267 images was created for the two observation geometries, covering a time span of almost 4 years, from January 2015 up to October 2018. As for S2 time series, the time sampling is not uniform as the second satellite (S1B) became available in October 2016. From that date on, two daily S1 passes are available every 6 days over the AOI, approximately at 6 am and 6 pm local time. The preprocessing applied to S1 collection backed up on the Graph Processing Tool distributed by ESA, and consists of four main steps: thermal noise removal, radiometric calibration, spatial speckle filtering (7×7 Lee-Sigma) and terrain correction. Sudden peaks in the temporal profile were smoothed using an additional Gaussian filtering step at pixel level. Finally, data were projected onto UTM reference to achieve a subpixel coregistration of the two collections. For each S1 acquisition, four products were initially generated: 1) VH and 2) VV radar reflectivities, 3) VH to VV ratio (VH/VV) and 4) dual-pol Radar Vegetation Index (RVI) calculated as ([Kim et al., 2012](#)):

$$\text{RVI} = \frac{4\text{VH}}{\text{VH} + \text{VV}}. \quad (9)$$

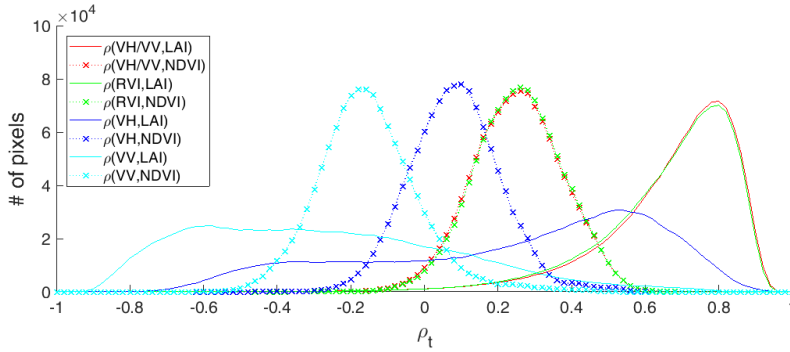


Figure 3: Histograms of Pearson's correlation coefficient ρ_t through time calculated per-pixel using all possible pairs of S2(NDVI,LAI) and S1(VV,VH,VH/VV,RVI) parameter time series over the AOI.

To trim down the time series length and further reduce speckle residual effects at once, the spatial correlation ρ_s between S1 ascending and descending SAR daily products was estimated using a 7×7 boxcar filter. The cumulative distribution of ρ_s calculated on 11 pairs of ascending-descending images throughout 2017 (Table 1) confirms that more than 97% of pixels have a correlation above 0.95 for VH and VV bands. The percentage is higher for VH/VV ratio, but the highest value is always obtained for RVI. This outcome agrees with [Veloso et al. \(2017\)](#), stating that for shallow incidence angles ($>35\text{-}40^\circ$) like in S1 observations the ascending and descending acquisitions over vegetation provide close responses in all bands ([Veloso et al., 2017](#)). Accordingly, S1 data acquired the same day were averaged.

3.4. Selection of active-passive vegetation descriptors

To demonstrate the potential of MOGP for optical-SAR gap filling, the pair of active-passive vegetation descriptors providing the highest correlation in time must be identified. The closeness of S1 and S2 information can be quantified using the Pearson's correlation coefficient ρ_t among all possible combination of optical (NDVI and LAI) and SAR (VV, VH, VH/VV, RVI) time series. The histograms in Figure 3 show that the highest values are obtained for VH/VV and LAI and for RVI and LAI, in line with the results in [Veloso et al. \(2017\)](#).

The spatial distribution of ρ_t between LAI and VV,VH and RVI are shown in Figure 4. We omitted VH/VV because changes with respect to RVI are negligible. RVI exhibits the highest ρ_t in most of the study area. The blueish strips in Figure 4c correspond to areas of low correlation, mainly pastureland. Here, volumetric scattering does not play an important

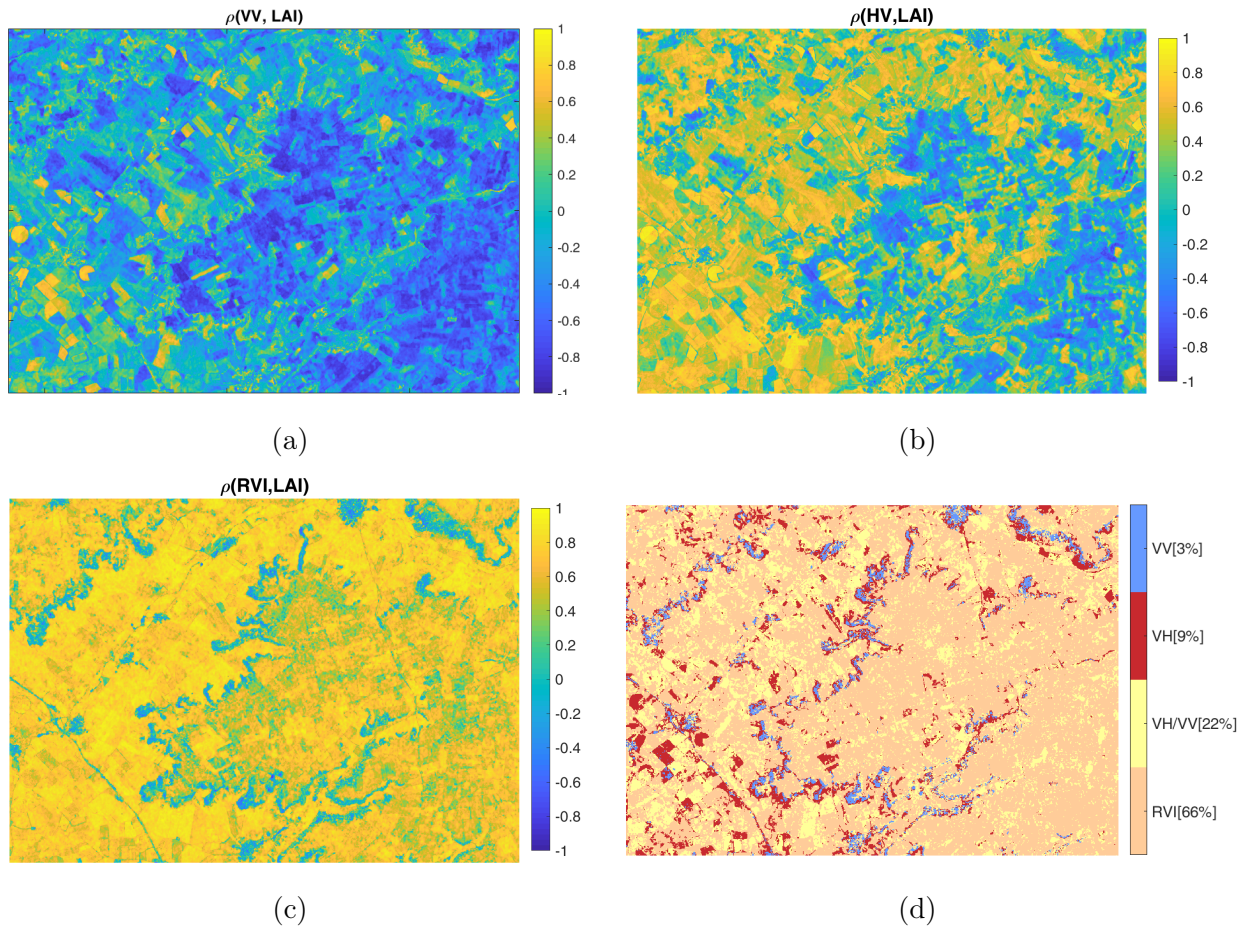


Figure 4: Spatial distribution of temporal correlation ρ_t between LAI and SAR vegetation descriptor time series - VV(a), VH(b), RVI (c) - and map of descriptor with the highest ρ_t (d) over the AOI.

role at C-band and surface backscattering dominates the SAR response, hence explaining the higher correlation with VV band (see Figure 4a) (Cloude, 2010). VV presents its highest values of ρ_t over some scattered parcels in the Southwest part of the AOI, which are mainly labeled as sunflower, but even there it is VH that outperforms the other three descriptors. Except for pasture, VV polarization tends to be less adequate for describing the crop stage evolution. All this information is summarized in Fig. 4d, which shows the product with the highest time correlation score at each pixel: RVI outperforms the other three descriptors over more than 65% of pixels, followed by VH/VV ratio in 23%, VH in 9% and finally VV in 3% of pixels. Based on these results, RVI and LAI time series are chosen as the optimal pair of crop phenology descriptors to be input to the proposed MOGP model for optical-SAR fusion.

4. Results

4.1. Temporal gap filling

To understand the functioning of MOGP, we first consider the case of a single parcel and analyze the features of its active-passive time series, interpret its trained model and assess its predictions. According to the land cover map product described in Gómez et al. (2018), it corresponded to wheat in 2016, beet in 2017 and again wheat in 2018.

4.1.1. Training time series

The images in Fig. 5 show the time evolution of LAI (a) and ascending/descending RVI (b) statistics (mean value and standard deviation) over the selected parcel. Many data are missing in S2 collection due to clouds (orange squares along the time axis of the upper image). A much denser sampling is provided by S1 along the whole observation period, as expected. For the second season, which offers the highest number of LAI samples, we sketched an example of the duration of the main crop phenological states (tillering, development, maturity, senescence/harvest) based on the evolution of LAI typically expected for each of them. In general, a high resemblance characterizes the active-passive collections. Concerning RVI, slight differences are observable between ascending (red) and descending (blue) profiles, mainly during 2016 wintertime (interval A). Soil anisotropic features, such as a specific plowing orientation, can induce backscattering differences under different observation geometries when the illuminating microwave interacts with the ground after propagating through the vegetation layer.

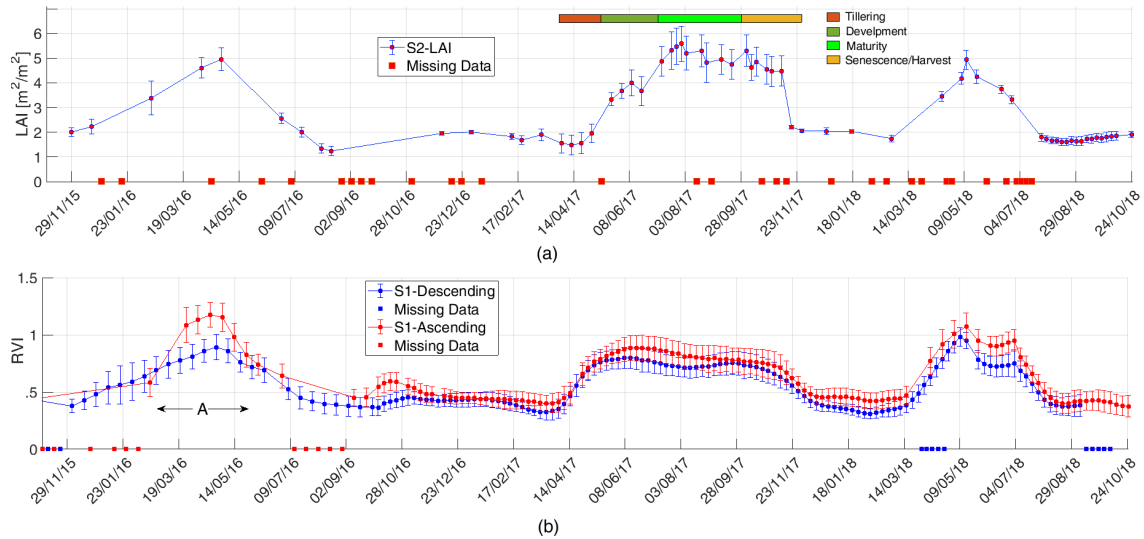


Figure 5: Statistical behavior (mean value and standard deviation) of LAI(a) and ascending(red) and descending(blue) RVI(b) time series over a selected parcel from November 2015 to end of October 2018. Inteval A in (b) indicates soil contribution to RVI impairing SAR co-/cross-polar balance between the two geometries. The main phenological stages of a crop are qualitatively sketch along the second season in (a), as qualitative reference.

Soil contributions impair the balance of energy between SAR co-polar and cross-polar bands expected over dense vegetation, explaining also RVI values higher than 1 (Szigarski et al., 2018). Nonetheless, this effect is unusual and non-representative of the general behavior, as demonstrated in Table 3.2. Accordingly, the RVI collections from ascending and descending orbits are merged and averaged when two daily samples are available. Finally, LAI and daily-averaged RVI time series are used for training.

4.1.2. Physical Interpretation of MOGP model

The LAI/RVI collections of Figure 5 are used to optimize the free parameters of the MOGP model defined in Section 2.4. Their value is reported in Table 2. A specific lengthscale parameter ℓ is obtained for each independent GP, one being significantly higher than the other. Recalling that ℓ defines the smoothing properties of the covariance kernel (Rasmussen, 2004), we refer to the GP with lower ℓ as LFGP (Low-Frequency), and to the other one as HFGP (High-Frequency). Note that the GP suffix has been omitted in Table 2 for ease of notation. According to the formulation in (8), each semi-definite rank-1 $[B]$ matrices is expressed as the outer product of the corresponding vector \mathbf{a} .

MOGP Optimized Parameters			
ℓ_{LF}	76.44	ℓ_{HF}	13.43
$[\mathbf{B}_{LF}] = \mathbf{a}_{LF} \mathbf{a}_{LF}^\top$	$\begin{bmatrix} 0.709 & 0.912 \\ 0.912 & 1.173 \end{bmatrix}$	$[\mathbf{B}_{HF}] = \mathbf{a}_{HF} \mathbf{a}_{HF}^\top$	$\begin{bmatrix} 0.180 & -0.013 \\ -0.013 & 0.001 \end{bmatrix}$
$\mathbf{a}_{LF}^\top = [\mathbf{a}_1^{LF} \ \mathbf{a}_2^{LF}]$	$\begin{bmatrix} 0.8420 & 1.0831 \end{bmatrix}$	$\mathbf{a}_{HF}^\top = [\mathbf{a}_1^{HF} \ \mathbf{a}_2^{HF}]$	$\begin{bmatrix} 0.4243 & -0.036 \end{bmatrix}$

Table 2: Main hyperparameters of the MOGP model trained with the LAI and RVI time series in Figure 5.

Each $[B]$ contains all the rules linking the corresponding GP to the two outputs, but its off-diagonal term b_{12} directly describes their degree of correlation with respect to that GP. As the off-diagonal element of $[B]_{LF}$ is close to 1, LFGP accounts for the common trends of LAI and RVI evolution. Moreover, being ℓ_{LF} significantly higher than ℓ_{HF} points out that only LFGP is able to describe the long-time changes of vegetation phenology. Conversely, ℓ_{HF} is low and the off-diagonal element of $[B]_{HF}$ close to zero, meaning HFGP fulfills essentially the task to absorb the short-time uncorrelated changes of the two outputs. The role of each GP can also be interpreted by examining the coefficients entering the linear combination in (7), which can be now rewritten as:

$$\begin{aligned}
 LAI(t) &= a_1^{LF} u_{LF}(t) + a_1^{HF} u_{HF}(t) \\
 RVI(t) &= a_2^{LF} u_{LF}(t) + a_2^{HF} u_{HF}(t),
 \end{aligned} \tag{10}$$

where $u_{LF}(t)$ and $u_{HF}(t)$ are the latent samples from LFGP and HFGP, respectively. Table 2 shows that $a_1^{LF} > 2a_1^{HF}$, implying the contribution of HFGP to LAI is of minor relevance. Because $a_2^{LF} \gg a_2^{HF}$, it becomes negligible for RVI. Then, LAI and RVI outputs generated by MOGP are essentially independent with respect to HFGP, and the prediction of LAI over cloudy dates mimics the local trend shown by the RVI output.

4.1.3. Prediction analysis of temporal profile

Once the MOGP model has been trained, it can be applied to predict LAI at any time. It is worth recalling from the sketch in Figure 1, that time is the only input to the model, and it is completely arbitrary. For instance, the use of the time vector corresponding to the union of the S2 (i.e. including the cloudy days) and S1 allows showing the potential of MOGP in blending the information of the two time series. This high prediction sampling makes it

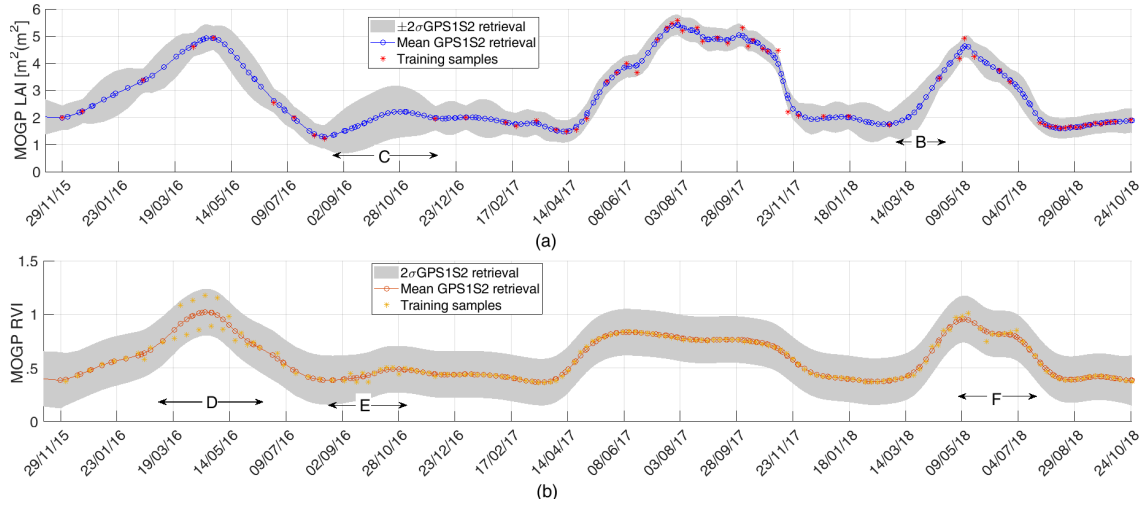


Figure 6: MOGP predictions (circles) of LAI (a) and RVI (b) on the union of S1 and S2 acquisition dates provided by the MOGP model trained on input time series (asterisks). The uncertainty of $\pm 2\sigma$ is represented by the boundary shade (grey) at any estimate. In (a), interval B indicates the realistic end of tillering dynamics obtained by fusing RVI information; interval C the higher uncertainty of LAI retrieval due to local differences between training samples of LAI (C) and of RVI (E) over the same period. In (b), intervals D and F indicate local inconsistencies between ascending and descending RVI samples likely due to anisotropic soil contributions.

easier to appreciate the capability of the technique to infer LAI missing information backing up on RVI time dynamics. Figure 6 shows the LAI (a) and RVI (b) predictions of the model examined in Section 4.1.2, along with their uncertainty. The two quantities are given by (5), with two different blocks of \mathcal{K} obtained by the training samples and the optimized model’s hyperparameters. The training samples are labeled by asterisks, the prediction mean values by circles, and their $\pm 2\sigma$ uncertainty by the boundary shade (grey).

LAI predictions generally match LAI training values, but the covariance filtering leads to a smoother time evolution over periods where training information is noisier, as it happens during the summer season in 2017. Note that smoother prediction profiles do not necessarily imply higher uncertainties if the sampling density allows discriminating noisy information. Over periods of densely sampled optical information, LAI training information dominates LAI prediction whereas RVI contributions are almost irrelevant. It is over periods with scarce optical samples, such as in 2016, that the advantage of the multioutput becomes clear. Instead of using only the LAI training samples, MOGP retrieves LAI using also the statistical correlation with RVI established during the training. MOGP is then able to reconstruct the transitional

LAI behaviors that have been undersampled by S2. For instance, the rise of LAI in March 2018 (interval B), which corresponds to the end of the tillering period and the so-called Start-Of-Season (SOS) (Jönsson and Eklundh, 2004), is reconstructed in a realistic way because this fast evolution was captured by RVI.

Concerning the uncertainty of the LAI prediction at a specific date, both the availability of samples and the local agreement between the two training collections play a role. The uncertainty is low when there is good match, but increases when only one parameter is available and some inconsistency is detected between them at the temporal extreme of the gap to be filled. The period labeled as interval C, between August and December 2016, shows a clear example. In relative terms, the increase of LAI value required to tie the two extremes of the gap ($>13\%$) is higher than RVI change ($<6\%$) around E. Then, the trend sensed by RVI must be distorted for S2 sample fitting, generating a higher uncertainty ($>1 m^2/m^2$) with respect to other filled intervals ($0.4 m^2/m^2$). With respect to uncertainty of RVI, the higher sampling density makes the prediction mean values match the training samples over most of the time series. The effects of noisy inputs is reduced by the covariance smoothing and the *coregionalization* link to LAI, forcing the output profile not to follow inconsistent patterns. Note for instance the samples in winter 2016 (interval D) following the trend of LAI and uncertainty limits defined by the inconsistency between ascending and descending orbits, or in fall 2016 and winter 2018 (intervals E and F, respectively). As for LAI output, RVI output is also influenced by the S2 training samples, although their effect is less evident.

A final remark on the information provided by MOGP is in order. The Standard GPR is a probabilistic nonparametric approach to regression and allows to compute uncertainties (predictive variance) of the inferred function. The gap filled time series provided by MOGP are obtained by transferring across domain/data sources not only the function predictions but also the uncertainties, allowing error quantification and uncertainty propagation by embedding the models in a higher level parameterization (Johnson et al., 2019).

4.1.4. Assessment of temporal profile

Here, we propose a quantitative assessment of MOGP predictions using the leave-one-image-out technique. It consists in taking a group of LAI time samples out of the training collections and assessing their predictions using these extracted values as reference. For this

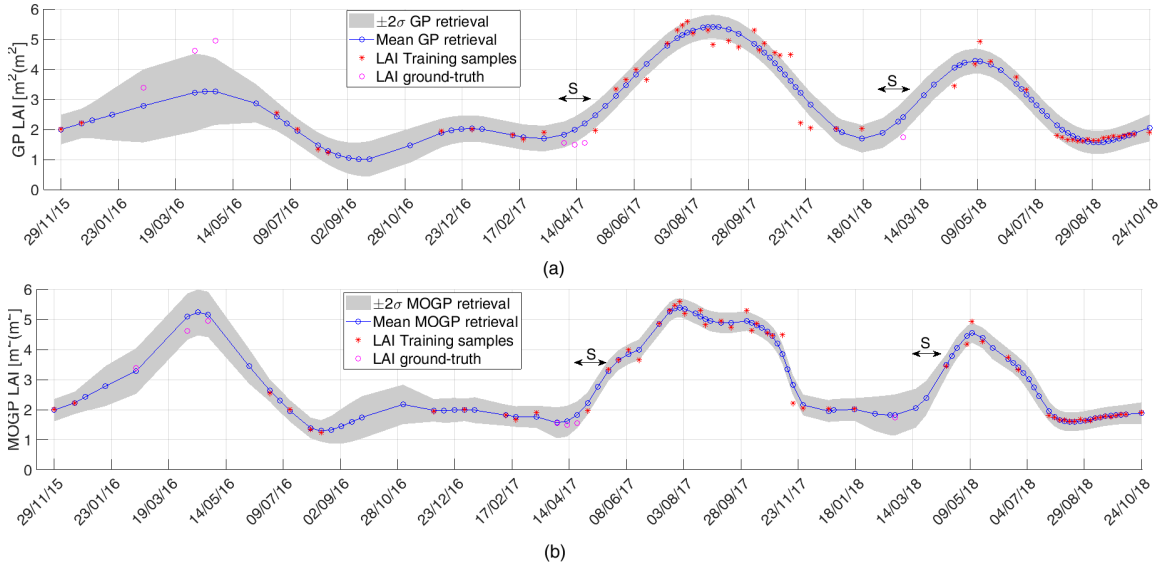


Figure 7: Assessment of standard GPR(a) and MOGP(b) predictions (blue circles) for data gap filling on S2 cloud-free captures (magenta) eliminated from training information (red asterisks) and here used as reference. The $\pm 2\sigma$ prediction uncertainty is represented by the boundary shade (grey) at any estimate. Intervals S in (a) and (b) evince the more realistic dynamics retrieved by MOGP during the stemming stages.

purpose, from the LAI time series in Figure 5a we eliminate 3 samples from February to April 2016, 3 samples from April to May 2017 and 1 sample in February 2018. Their elimination generates 3 artificial gaps ranging from 25 up to 90 days, which exemplify realistic high-latitude S2 sampling conditions due to the prominent cloud cover. To highlight the benefits of the fusion approach, MOGP retrievals are also compared to estimations of standard GPR trained on the reduced collection of the LAI samples (Section 2.1) As shown in Appendix A, GPR provided the best assessment performance among a set of conventional and advanced interpolation techniques. The result of GPR and MOGP retrievals are shown in Figure 7. The predictions have been carried out only on the dates of S2 nominal captures to facilitate the identification of the samples useful for the assessment. Yet, it is worth stressing again that there is no limitation in the time sampling of the prediction output provided by the MOGP trained model.

The lower capability of GPR to reconstruct LAI over long time data gaps can be easily observed for winter-spring 2016; the true phenological evolution of the crop (magenta circles) is completely lost because all missing values are significantly underestimated. Moreover, the predictions are characterized by a higher uncertainty and, consequently, a lower reliability.

The retrieval over the other assessment dates generally overestimates the LAI true value, with a consequent anticipation of the stemming stage (indicated with an S in Figure 7). Note that the true values fall often outside the 2σ significance interval. Conversely, the simultaneous use of SAR-based information allows a more correct retrieval of crop phenological stages, within short and long data gaps. In most cases, the mean LAI estimation provided by MOGP almost coincides with the S2-based reference, causing no time shift or stretching in the description of the crop seasons. The quantitative assessment of the 7 predictions carried out by GPR and MOGP provides $R^2 = 0.90$ and $RMSE = 0.95m^2/m^2$ for the former, $R^2 = 0.99$ and $RMSE = 0.24m^2/m^2$ for the latter. Another observation is that the LAI retrieval carried out over the longest time gap relies mainly on SAR data alone, while the contribution from optical data is marginal. Here, the meaning of passive-active data fusion is likely lost at local scale. Nonetheless, it is only thanks to the synergistic rules learned by MOGP over the fused active-passive complete time series that inferring the LAI behavior from RVI time evolution becomes feasible.

4.2. Spatiotemporal gap filling

The noteworthy results provided by MOGP over the selected parcel underpin its capability to merge profitably the active-passive information, and reconstruct otherwise lost details of the vegetation phenology. Yet, its performances are deeply related to the time resemblance of the training time series. As the areas crop type often differs across multiple crop seasons, it is interesting to analyze the behavior of MOGP when trained using long time series over time-heterogeneous areas, and at pixel instead of parcel level.

4.2.1. Spatial patterns of MOGP trained models

Keeping in mind the interpretation of the MOGP model in Section 4.1.2, here we extend the analysis to the spatial domain. An independent model is trained for each pixel of the AOI using its corresponding LAI and RVI complete time series. Figure 8a,b and c show the spatial distribution and the histograms of ℓ_{LF} and ℓ_{HF} . The results over vegetated areas confirm MOGP identifies a LFGP accounting for the information shared between the two outputs, and a HFGP explaining their local differences along time. ℓ_{LF} varies from 40 to 80 days over croplands, being this range consistent with the time correlation expected for vegetation

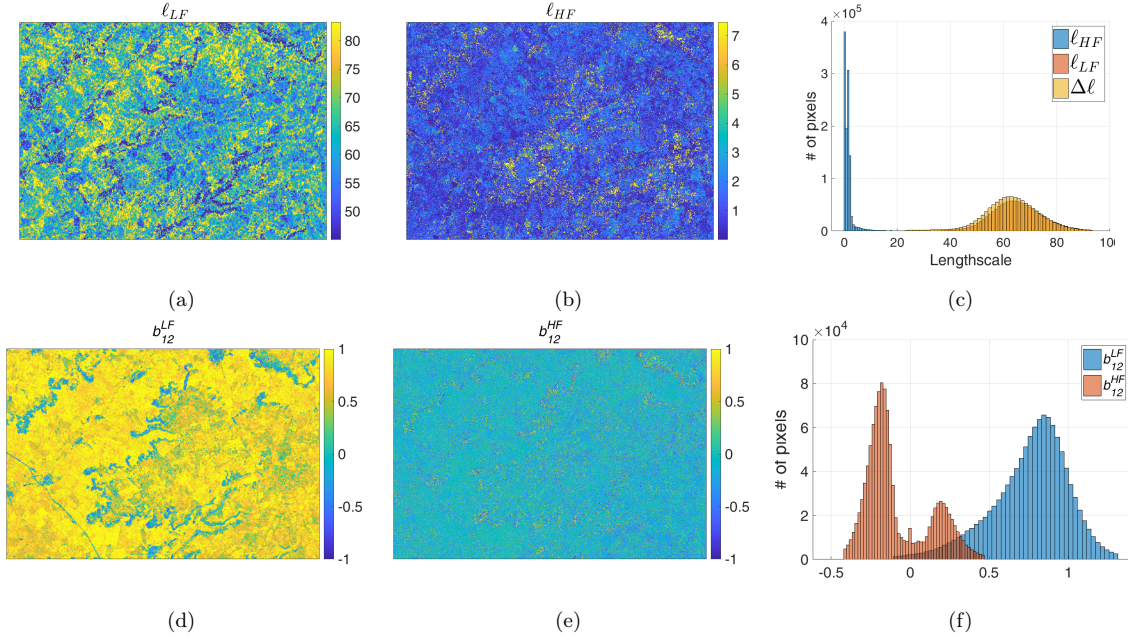


Figure 8: Spatial distribution over the AOI and histograms over crop areas of ℓ parameter for LF and HF (a,b and c in upper panel), and of b_{12}^{LF} and b_{12}^{HF} (d,e,f in lower panel).

phenology descriptors. Pasture lands and man-made surfaces such as road and urban areas, which present low ℓ_{LF} values in Figure 8a, have not been included in any quantitative statistics hereafter presented. Higher ℓ_{LF} values are generally associated with barley and wheat fields, although the crop rotation applied during the three years covered by the training complicates the identification of time-homogeneous crop regions. For each crop pixel, ℓ_{LF} provides the optimum time-scale of the covariance kernel to follow the vegetation dynamics throughout the seasons covered by the training; the values of ℓ_{HF} reflect the shorter time-scale of HF contributions to account for local behaviors. The almost perfect overlapping between the histograms of ℓ_{LF} and $\ell_{LF} - \ell_{HF}$ ($\Delta\ell$) in Figure 8c demonstrates this high-low frequency dichotomy holds for almost all the pixels within the scene.

We can draw some additional considerations from the spatial distribution of b_{12}^{LF} and b_{12}^{HF} , shown in Figures 8d and 8e. Their histograms are also given in 8f to facilitate their comparison. High values of b_{12}^{LF} characterize most of the crop polygons, with a slight lower distribution on the East part of the AOI. The results confirm that LF carries the shared information of the two outputs regarding the vegetation structure, which explains also the resemblance between

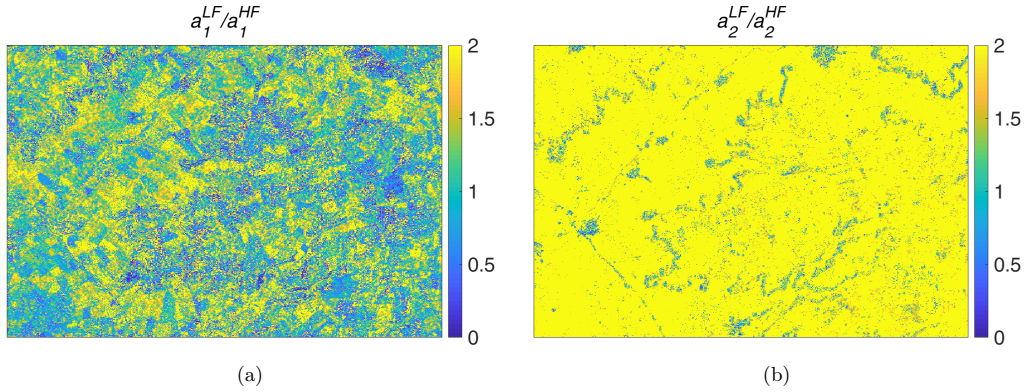


Figure 9: Spatial distribution of the ratios between high- (a) and low-frequency (b) coefficients in (10).

b_{12}^{LF} and $\rho_t(RVI, LAI)$ in Figure 4c. Following a similar reasoning, we can state that the two outputs are generally more independent with respect to HFGP contributions.

A further step in the analysis is the study of the ratios between their coefficients in (10), i.e. a_1^{LF}/a_1^{HF} and a_2^{LF}/a_2^{HF} . Their spatial maps are shown in images (a) and (b) of Figure 9, respectively. $a_2^{LF} \gg a_2^{HF}$ indicates that LFGP always dominates the linear combination providing RVI output, and indirectly that the SAR data time-smoothing preprocessing was effective (Section 3.3). An alternative interpretation is that RVI output information is fully contained in LAI output.

For LAI, the contribution balances in (10) becomes more complex because LFGP does not prevail everywhere. The spatial distribution of Figure 9a reveals that 1) for about 60% of pixels within the AOI holds the condition $a_1^{LF} > a_1^{HF}$, 2) only for 20% of them it keeps above 1.5 and makes LFGP dominant. For the remaining 40% pixels the contribution of HFGP is significant, and more than its half even dominant, i.e. $a_2^{LF}/a_2^{HF} < 0.75$. For these latter pixels, LAI time series contains non-negligible high-frequency details at higher frequency that are not sensed by RVI. As a consequence, RVI capability to facilitate LAI data gap filling becomes significantly lower.

4.2.2. Spatial prediction analysis

Following the leave-one-image-out assessment strategy proposed in Section 4.1, the same S2 acquisitions were left out for MOGP and GPR training at pixel level. For each assessment date, three LAI maps are created: the predictions of MOGP and GPR models and the map obtained from the original S2 capture (Amin et al., 2018), which is used as reference for the

assessment.

The quantitative comparison between reference and estimation is provided in terms of error histograms and scatter plot histograms, for two pixel selection criteria: 1) crop pixels fulfilling the condition $a_1^{LF}/a_1^{HF} > 1.5$, assuring RVI contribution are dominant for the LAI interpolation; 2) all crop pixels available. For convenience, only the maps corresponding to longer gaps of 90 and 50 days are presented here, and assessed using the first pixel selection criterion. The results using both selection criteria for all the eliminated dates are presented in Section 4.2.3, along with a crop type analysis of MOGP and GPR prediction performance.

Scenario 1: long temporal gap. The first gap case being studied is the longest one: 90 days between 1/17 and 4/14 in 2016. The missing dates are 2/17, 4/7 and 4/27. Figure 10 shows the results obtained for the first and the last dates. Qualitatively, the comparison between reference (1st column) and retrieved maps indicates that MOGP (2nd column) provides better LAI estimations than GPR (3rd column). GPR predictions tend to overestimate LAI, often providing unlikely values higher than 7. Conversely, MOGP prevents improbable predictions but slightly underestimates LAI values, as shown by the positive offset of the error histograms. The histograms indicate also a significantly lower dispersion of the errors given by MOGP, confirmed by RMSE values. A good match between reference and MOGP retrievals is obtained for LAI < 3. Similar conclusions can be drawn by comparing the values of R^2 , higher for MOGP even if quite low in absolute terms, and RMSE.

Scenario 2: moderate temporal gap. The retrievals shown in Figure 11 correspond to 4/12, the central date within the 50-day time gap from 3/13 to 5/2 in 2017. The predictions provided by the two approaches are alike. From the statistical point of view, the error dispersion is almost identical. The values of R^2 ranges around 70% for both approaches, with MOGP slightly better than GPR; RMSE values are similar too. As already observed for the long temporal gap case, GPR tends to overestimate to unreliable values, whereas MOGP usually underestimates the highest values of LAI appearing in the reference maps. The main reason is probably that the MOGP solution is tied to the RVI temporal dynamics, which prevents the sudden appearance of LAI peaks induced by noisy estimates from S2 data. As an example, note the unlikely LAI evolution given by GPR on the parcels in the down-left part of AOI (yellow rectangle in Figure 2), whose zooms are shown in Figure 12. The overall values of LAI

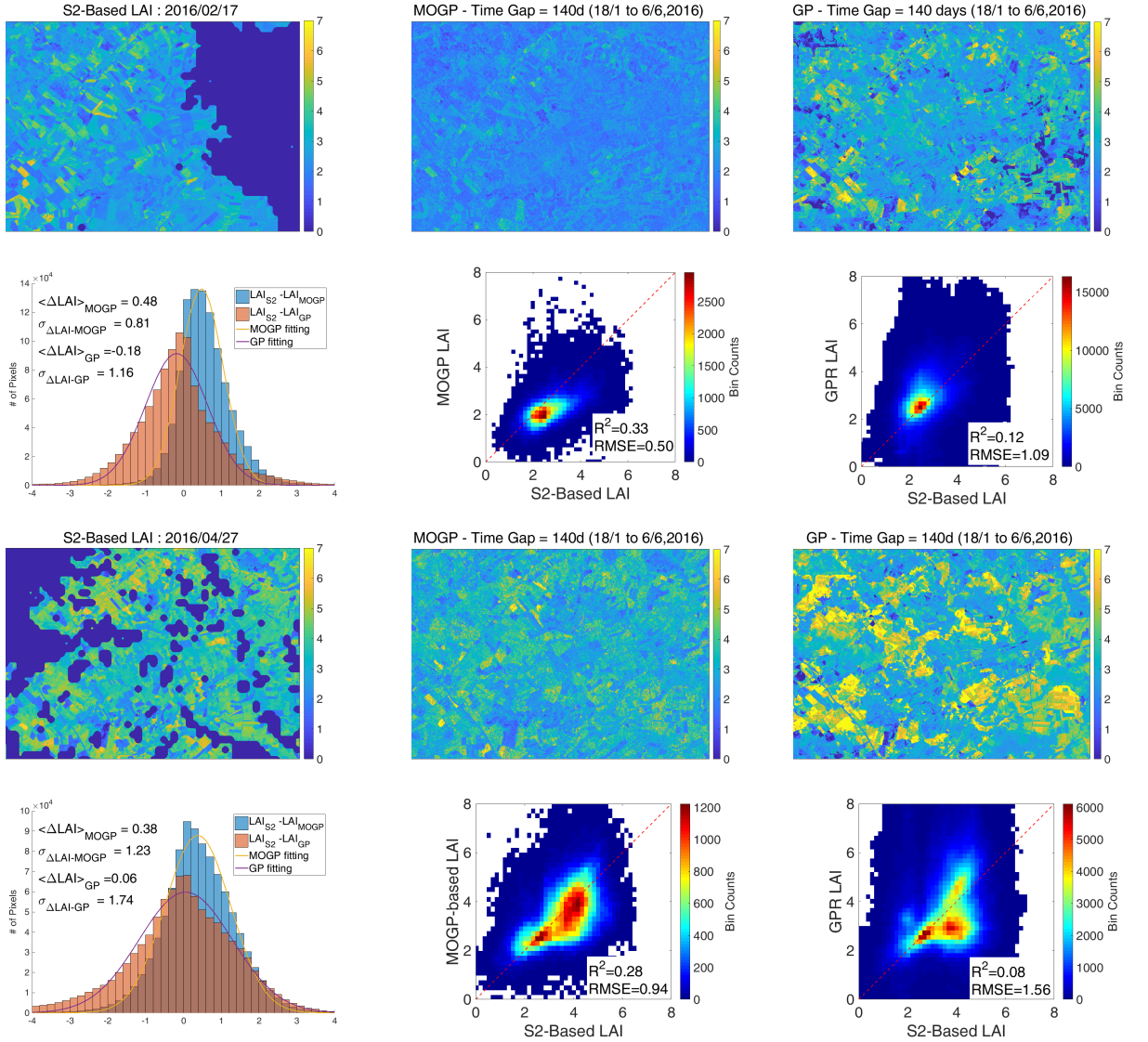


Figure 10: LAI maps from S2 image (reference), MOGP and standard GP, error histograms and scatter plots for two dates: 2016/2/17 and 2016/04/27 (90 days gap from 2016/1/18 to 2016/4/17).

predicted by GPR range between 0 and 7, with local irregular changes too high to be plausible in less than one month (up to almost 7 and below 5 in 3 weeks). Over the same area, MOGP provides a gradually increase response along time, which can be considered more realistic.

4.2.3. Assessment of retrieved maps

The performance of MOGP is strictly related to the existence of a favorable relationship between a_1^{HF} and a_1^{LF} , which represents the core hypothesis for any active-passive synergy.

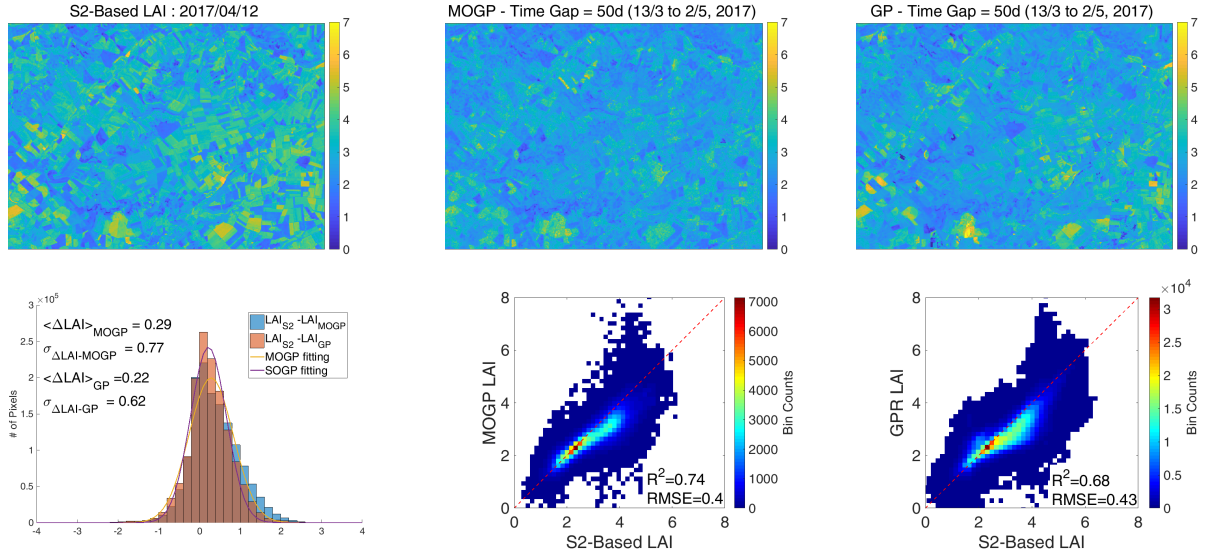


Figure 11: LAI maps from S2 image (reference), MOGP and standard GP, error histograms and scatter plots for 2017/4/12 (50 days gap from 2017/3/13 to 2017/5/2).

Prediction vs S2-based LAI

	2016/02/17	2016/04/07	2016/04/27	2017/04/02	2017/04/12	2017/04/22	2018/02/26
R^2_{MOGP}	<u>0.29</u> (0.33)	<u>0.20</u> (0.19)	<u>0.29</u> (0.26)	<u>0.56</u> (0.70)	<u>0.58</u> (0.74)	<u>0.49</u> (0.71)	<u>0.25</u> (0.35)
R^2_{GPR}	<u>0.12</u> (0.12)	<u>0.06</u> (0.08)	<u>0.08</u> (0.08)	<u>0.67</u> (0.67)	<u>0.68</u> (0.68)	<u>0.70</u> (0.70)	<u>0.40</u> (0.40)
$\text{RMSE}_{\text{MOGP}}$	<u>0.44</u> (0.50)	<u>0.80</u> (0.90)	<u>0.85</u> (0.94)	<u>0.42</u> (0.41)	<u>0.44</u> (0.40)	<u>0.55</u> (0.42)	<u>0.36</u> (0.44)
RMSE_{GPR}	<u>1.12</u> (1.09)	<u>1.75</u> (1.70)	<u>1.62</u> (1.56)	<u>0.44</u> (0.43)	<u>0.46</u> (0.43)	<u>0.45</u> (0.41)	<u>0.50</u> (0.50)

Table 3: R^2 and RMSE [m^2/m^2] of LAI maps from S2 image (reference) vs MOGP and GPR over all the vegetated pixels (blue) and only pixels fulfilling $a_1^{LF}/a_1^{HF} > 1.5$ (black).

The results summarized in Table 3 underlines exactly this point. Including all the pixels corresponding to crop areas in the assessment leads to R^2 values of MOGP predictions always lower than those obtained with the pixels fulfilling the condition $a_1^{LF}/a_1^{HF} > 1.5$. Almost the same happens with RMSE, even if the magnitude of the change is lower. Conversely, the results for GPR are practically identical, confirming the samples considered for the two analyses comprehend all possible cases.

MOGP retrievals present higher errors over low LAI areas, which typically corresponds to the beginning of the crop season (tillering) such as samples on 2016/2/17 and 2018/02/26. A possible explanation lies in the different properties of vegetation cover the two sensors are able to capture: its greenness for optical and its real volumetric structure, i.e. fresh biomass, for SAR. Albeit these two quantities are strictly related, depending on the land cover they may

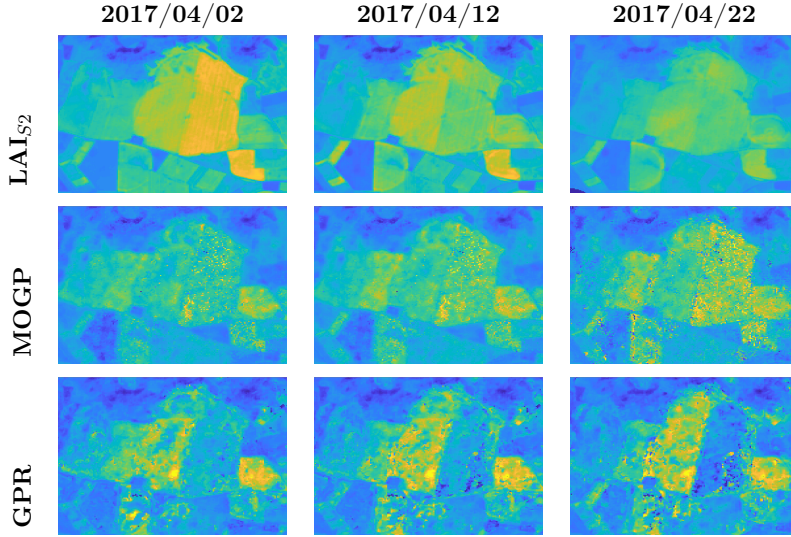


Figure 12: Comparison of LAI maps from S2 image (reference), MOGP and standard GP over a subset of AOI (yellow rectangle in Figure 2) corresponding to 4/2, 4/12 and 4/22 within the 50 days gap from 2017/3/13 to 2017/5/2. LAI evolution provided by GPR is more unlikely than MOGP’s results.

lead to slightly dissimilar estimation of LAI as the former usually anticipates the latter. From this point of view, the importance of the final findings summarized in Table 3 is twofold. On the one hand, they demonstrate the existence of a stochastic relationship between the time series of optical and radar vegetation descriptors among areas characterized by a dominant LFPG. On the other hand, they allow identifying crop areas where common long-time patterns between S2-LAI and S1-RVI time series are barely detectable.

To look further into this last issue, we analyze the performance of the synergy methodology per crop type. A long time series is required to optimize the free parameters of the model at pixel level, but the crop rotation may reduce MOGP performance in case of seasonal correlation changes. In order to workaround this issue, we consider only the pixels fulfilling the condition $a_1^{LF}/a_1^{HF} > 1.5$, which guarantees the active-passive synergy is profitable. For each assessment date, we used the corresponding land cover map to select pixels belonging to the same class, and calculated R^2 and RMSE.

We identified 13 permanent classes along the three years, except for rye present for years 2017 and 2018. Information about the classes, their distribution in space and time, and the assessment results in terms of R^2 and RMSE are detailed in Tables 4 and 5, respectively.

Taking into consideration R^2 in Table 4, we observe a dominance of red colors over the long

R^2	2016/02/17			2016/04/07		2016/04/27		2017/04/02			2017/04/12		2017/04/22		2018/02/26		
	LCMap(%)	MOGP	GPR	MOGP	GPR	MOGP	GPR	LCMap(%)	MOGP	GPR	MOGP	GPR	MOGP	GPR	LCMap(%)	MOGP	GPR
Wheat	30.2	0.287	0.148	0.072	0.015	0.102	0.036	25.7	0.487	0.578	0.549	0.694	0.518	0.728	29.5	0.223	0.251
Maize	0.2	0.121	0.028	0.355	0.393	0.811	0.333	0.1	0.854	0.829	0.88	0.854	0.928	0.886	0.2	0.812	0.888
Barley	32.2	0.221	0.04	0.058	0.009	0.071	0.015	37.4	0.613	0.664	0.642	0.72	0.606	0.737	31.6	0.185	0.24
Rye	0.0	0	0	0	0	0	0	0.2	0.781	0.822	0.766	0.848	0.719	0.861	0.3	0.232	0.468
Oats	0.2	0.148	0.564	0.293	0.424	0.487	0.163	0.0	0.414	0.121	0.515	0.195	0.638	0.339	0.4	0.453	0.472
Sunflower	1.5	0.253	0.08	0.154	0.048	0.145	0.076	1.3	0.522	0.393	0.596	0.438	0.545	0.383	2.2	0.349	0.519
Rapeseed	0.8	0.276	0.288	0.075	0.373	0.061	0.006	0.8	0.493	0.534	0.199	0.331	0.295	0.351	1.2	0.579	0.564
Other leguminous	7.0	0.041	0.014	0.045	0.006	0.06	0.006	6.7	0.399	0.152	0.5	0.236	0.544	0.39	8.4	0.028	0.082
Greenpeas	2.8	0.069	0	0.315	0.066	0.381	0.103	3.4	0.624	0.533	0.686	0.621	0.644	0.696	3.3	0.047	0.199
Alfalfa	0.4	0.417	0.586	0.281	0.241	0.339	0.219	0.7	0.603	0.557	0.661	0.589	0.62	0.615	1.2	0.497	0.611
Foragecrops	1.6	0.315	0.062	0.127	0.073	0.115	0.009	0.9	0.566	0.544	0.599	0.611	0.546	0.699	0.0	0.671	0.793
Beet	1.4	0.173	0.003	0.135	0.07	0.203	0.065	1.4	0.064	0.081	0.171	0.186	0.187	0.477	1.2	0.004	0.017
Potatoes	0.2	0.524	0.252	0.002	0.046	0.427	0.704	0.2	0.087	0.156	0.024	0.191	0.367	0.221	0.2	0.559	0.775

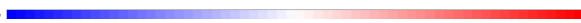
$\Delta R^2 = R^2_{MOGP} - R^2_{GPR}$: -0.5  0.5

Table 4: Per-class R^2 calculated over pixels fulfilling the condition $a_1^{LF}/a_1^{HF} > 1.5$. The cell background is proportional to MOGP and GPR performance difference in a blue-white-red colormap. Blueish tones indicate R^2_{MOGP} is lower than R^2_{GPR} ; reddish tones the other way around; white color denotes negligible differences.

data gap (2016), meaning MOGP generally provides higher values than GPR. Higher absolute values are obtained for Oats, Greenpeas and Alfalfa; the highest performance is obtained over Maize, even if only for a fully developed crop at the end of April 2016. As important as R^2 are also the values of RMSE, reported in Table 5. The residuals over the long time data gap are significantly higher for GPR than MOGP, with the blueish color characterizing all the crop types. Concerning shorter data gaps, the two approaches present similar performances, as already pointed out in Section 4.2.2. Still, some classes such as Oats, Greenpeas, Alfalfa and Maize, present a higher score for the synergistic approach. Sunflowers deserves a specific mention: all the artificial gaps lie from winter to spring time, when this crop type is at an early stage of development. Superior results from the active-passive synergy are expected over cloudy early-summer periods, when their development is more advanced.

5. Discussion

Establishing a physically interpretable link between active and passive time series over vegetated areas becomes feasible using MOGP modeling. An absolute novelty of the solution we proposed is that the parameters of the trained model implicitly predict the meaningfulness of any fusion approach: they quantify the amount of information shared between the two time series and rule the interaction of low- and high-frequency GPs for output reconstruction. The LAI data gap filling described in this work is just an example of MOGP possible applications.

RMSE	2016/02/17		2016/04/07		2016/04/27		2017/04/02			2017/04/12		2017/04/22		2018/02/26			
	LCMap(%)	MOGP	GPR	MOGP	GPR	MOGP	GPR	LCMap(%)	MOGP	GPR	MOGP	GPR	MOGP	GPR	LCMap(%)	MOGP	GPR
Wheat	30.2	0.552	1.059	0.948	1.45	1.001	1.313	25.7	0.442	0.367	0.422	0.342	0.449	0.345	29.5	0.435	0.398
Maize	0.2	0.627	0.436	0.77	0.889	0.536	0.906	0.1	0.351	0.358	0.407	0.44	0.361	0.463	0.2	0.255	0.194
Barley	32.2	0.427	1.002	0.786	1.606	0.879	1.517	37.4	0.398	0.422	0.387	0.406	0.42	0.389	31.6	0.452	0.548
Rye	0.0	0	0	0	0	0	0	0.2	0.343	0.338	0.338	0.31	0.34	0.279	0.3	0.465	0.286
Oats	0.2	0.807	0.883	0.755	1.478	0.946	1.756	0.0	0.536	0.775	0.589	0.784	0.548	0.711	0.4	0.374	0.466
Sunflower	1.5	0.383	0.744	0.425	1.061	0.434	0.763	1.3	0.303	0.31	0.305	0.353	0.362	0.415	2.2	0.345	0.298
Rapeseed	0.8	0.613	1.338	0.764	1.551	1.255	2.11	0.8	0.759	0.739	0.978	0.91	0.918	0.84	1.2	0.636	0.532
Other leguminous	7.0	0.474	1.261	0.718	2.207	0.824	1.8	6.7	0.257	0.49	0.254	0.46	0.262	0.376	8.4	0.434	0.407
Greenpeas	2.8	0.414	1.232	0.656	2.057	0.749	2.129	3.4	0.273	0.316	0.281	0.311	0.322	0.29	3.3	0.392	0.395
Alfalfa	0.4	0.953	0.945	1.102	2.358	1.193	2.196	0.7	0.48	0.356	0.431	0.357	0.447	0.359	1.2	0.47	0.389
Foragecrops	1.6	0.472	1.724	0.675	2.916	0.779	3.026	0.9	0.254	0.298	0.262	0.297	0.291	0.276	0.0	0.297	0.278
Beet	1.4	0.59	0.707	0.694	1.128	0.601	1.141	1.4	0.494	0.465	0.512	0.513	0.595	0.472	1.2	0.426	0.572
Potatoes	0.2	0.59	0.973	0.764	0.85	0.588	1.137	0.2	0.266	0.458	0.288	0.479	0.29	0.458	0.2	0.68	0.357


$\Delta_{RMSE} = RMSE_{MOGP} - RMSE_{GPR}$ -1.5  1.5

Table 5: Per-class RMSE [m^2/m^2] calculated over pixels fulfilling the condition $a_1^{LF}/a_1^{HF} > 1.5$. The cell background is proportional to (MOGP,GPR) performance difference in a blue-white-red colormap. Blueish tones indicate RMSE is lower for MOGP than for GPR; reddish tones the other way around; white color denotes negligible differences.

The strength of the two time series synergy strictly depends on the crop type, being some crops more prone to be well characterized by RVI (such as oats, wheats or maize), but also on crop-stage. All the same, the SAR information extracted by MOGP is key to reduce prediction uncertainties with respect to advanced single-output regression over long time data gaps.

Concerning the absolute values of R^2 , higher performances are desirable: a best score of 74% might be considered modest from an absolute point of view, except for the 81% over maize within the long time data gap. Still, the estimation of vegetation parameters from single optical acquisition is notoriously affected by atmospheric correction residual errors and surface anisotropy (Jonsson and Eklundh, 2002). These effects make the original time series unfit for any seasonality information extraction, unless smoothing procedures and outlier filtering are previously applied (Jönsson and Eklundh, 2004). Then, our assessment based on direct LAI retrievals from S2 captures is likely to underestimate the real performance of MOGP (and GPR), due to the smoothing process performed by the covariance kernel. This means that differences between reference and validation do not always represent a worse estimation of true LAI. Having at disposal ground-truth information about season length, start-of-season and end-of-season for different crops for instance (Richardson et al., 2013), a different assessment could be envisaged.

Some limitations of the proposed approach must be also stressed, related to either its theoretical formulation or the specific implementation we carried out in this work. The main

theoretical limitation of MOGP is that it is unable to take into account possible time-shift between even highly correlated time series. If changes appear with a delay in the two sources of information, the efficiency of the reconstruction is affected in a way proportional with the magnitude of the time separation. Similarly, contraction or dilation effects of similar patterns cannot be exploited properly for the reconstruction, even if less probable.

Another weakness of the MOGP is its high computational cost, which makes it inefficient if the per-pixel training is applied at large scale. A more efficient usage of MOGP should exploit spatial homogeneities. Polygons from land cover maps, if available, enable to reduce the computational time by moving from a pixel-wise to an object-oriented approach, if one accepts to lose details about the spatial heterogeneity of each polygon. Yet, the homogeneity of the same polygon must be checked when dealing with multiple-year time series, if we want to avoid the average of different crop types in space or time. The stationarity of the processes entering MOGP is not always fulfilled: LFGP stops being dominant and the identification of a statistical linking modeling covering the whole time series is not straightforward. Even if the crop-based assessment circumvented this problem by selected only those pixels showing a high active-passive correlation, the real performance of MOGP are likely underestimated. A potential improvement is the estimation of crop-specific Coregionalization matrices via crop type space (multiple polygons) and time (multiple years) training. This knowledge could be applied at pixels level in a transfer learning framework, if an yearly-updated land cover map is available. Using crop type precalculated $[\mathbf{B}]$ matrices, less samples are required for the estimation of the remaining free parameters, and processing single seasonalities for gap filling purposes becomes feasible. This new approach is expected to help deal with shorter time series and, to some extent, speed up the model training process. In fact, the main bottleneck represented by the inversion of \mathcal{K} is still present. Yet, all these follow-up studies go beyond the purpose of this work, whose main objectives have been 1) demonstrating the capability of MOGP to establish active-passive time series synergy through a statistically interpretable model, and 2) providing a practical example of MOGP for tackling a crucial problem of spaceborne vegetation monitoring, i.e. filling the long time-gaps of optical vegetation descriptors induced by clouds.

6. Conclusions

The MOGP technique introduced in this work represents an innovative approach in the remote sensing community for establishing a fusion between optical and SAR information. Unlike other black-box machine learning solutions, the interpretation of the MOGP model is easy: the two imageries are modeled as combinations of independent GPs and their influence in the final prediction is weighted by the corresponding *coregionalization* matrix. The approximations held in this study constitutes a first demonstration of MOGP capability to extract information shared between collections of LAI and RVI acquisitions. The results demonstrate the capability of MOGP for retrieving missing LAI values, improving the prediction of standard GP over short-time gaps (R^2 of 74% vs 68%) and especially over long-time gaps (R^2 of 33% vs 12%, RMSE of 0.5 vs 1.09). The method we proposed always guarantees that the LAI time series obtained as output follows RVI time evolution if no optical sample is available over long periods, keeping the solution tied to real measurements. The crop-specific analysis reveals the synergy is profitable for most crops, even if MOGP performance is crop type as well as crop stage dependent. Specially maize, but also wheat, oats, rye and barley, can profit from the LAI-RVI synergy. For beet or potatoes results are less encouraging, but alternative active descriptors to RVI should be explored. In conclusion, active-passive sensor fusion with MOGP represents a novel and promising approach to cope with crop monitoring over cloud-dominated areas.

Further studies are now required to advance towards a more efficient usage of MOGP. For instance, spatial homogeneities can be exploit to move from a pixel-wise to an object-oriented approach, accepting to lose the possible spatial heterogeneity within the polygon. Other two aspects to be examined are including multiple SAR descriptors to MOGP model over specific crop types, and exploring model training over single-seasonality. However, shorter observation periods imply having fewer time samples to train a more complex model. All these aspects must be carefully studied and motivate future analysis.

7. Acknowledgement

The research leading to these results has received funding from the European Union’s Horizon 2020 Research and Innovation Programme, under Grant Agreement no 730074. Luca

Pipia and Jochem Verrelst were supported by the European Research Council (ERC) under the ERC-2017-STG SENTIFLEX project (grant agreement 755617). Gustau Camps-Valls was supported by ERC under the ERC-COG-2014 SEDAL (grant agreement 647423). GCV and JMM acknowledge the funding received from the Spanish Ministry of Economy and Competitiveness (MINECO) and FEDER co-funding through the projects TIN2012-38102-C03-01 and TIN2015-64210-R.

References

- Alvarez, M.A., Rosasco, L., Lawrence, N.D., et al., 2012. Kernels for vector-valued functions: A review. *Foundations and Trends® in Machine Learning* 4, 195–266.
- Amarsaikhan, D., Ganzorig, M., Ache, P., Blotvogel, H., 2007. The integrated use of optical and InSAR data for urban land-cover mapping. *International Journal of Remote Sensing* 28, 1161–1171.
- Amin, E., Verrelst, J., Rivera-Caicedo, J.P., Pasqualotto, N., Delegido, J., Verdú, A.R., Moreno, J., 2018. The Sensagri Sentinel-2 Lai Green and Brown product: from algorithm development towards operational mapping, in: *IGARSS 2018-2018 IEEE International Geoscience and Remote Sensing Symposium*, IEEE. pp. 1822–1825.
- Bacour, C., Bréon, F.M., Maignan, F., 2006. Normalization of the directional effects in NOAA-AVHRR reflectance measurements for an improved monitoring of vegetation cycles. *Remote Sensing of Environment* 102, 402–413.
- Baret, F., De Solan, B., López-Lozano, R., Ma, K., Weiss, M., 2010. GAI estimates of row crops from downward looking digital photos taken perpendicular to rows at 57.5 zenith angle: Theoretical considerations based on 3D architecture models and application to wheat crops. *Agricultural and Forest Meteorology* 150, 1393–1401.
- Baup, F., Fieuzal, R., Betbeder, J., 2015. Estimation of soybean yield from assimilated optical and radar data into a simplified agrometeorological model, in: *Geoscience and Remote Sensing Symposium (IGARSS), 2015 IEEE International*, IEEE. pp. 3961–3964.

- Berger, M., Moreno, J., Johannessen, J., Levelt, P., Hanssen, R., 2012. ESA's sentinel missions in support of earth system science. *Remote Sensing of Environment* 120, 84–90. doi:[10.1016/j.rse.2011.07.023](https://doi.org/10.1016/j.rse.2011.07.023).
- Boles, S.H., Xiao, X., Liu, J., Zhang, Q., Munkhtuya, S., Chen, S., Ojima, D., 2004. Land cover characterization of Temperate East Asia using multi-temporal VEGETATION sensor data. *Remote Sensing of Environment* 90, 477–489.
- Bousbih, S., Zribi, M., Lili-Chabaane, Z., Baghdadi, N., El Hajj, M., Gao, Q., Mougenot, B., 2017. Potential of Sentinel-1 Radar Data for the Assessment of Soil and Cereal Cover Parameters. *Sensors* 17, 2617.
- Cammalleri, C., Anderson, M., Gao, F., Hain, C., Kustas, W., 2014. Mapping daily evapotranspiration at field scales over rainfed and irrigated agricultural areas using remote sensing data fusion. *Agricultural and forest meteorology* 186, 1–11.
- Campos-Taberner, M., García-Haro, F.J., Camps-Valls, G., Grau-Muedra, G., Nutini, F., Crema, A., Boschetti, M., 2016. Multitemporal and multiresolution leaf area index retrieval for operational local rice crop monitoring. *Remote Sensing of Environment* 187, 102–118.
- Camps-Valls, G., Gómez-Chova, L., Muñoz-Marí, J., Rojo-Álvarez, J.L., Martínez-Ramón, M., 2008. Kernel-based framework for multitemporal and multisource remote sensing data classification and change detection. *IEEE Transactions on Geoscience and Remote Sensing* 46, 1822–1835.
- Camps-Valls, G., Jung, M., Ichii, K., Papale, D., Tramontana, G., Bodesheim, P., Schwalm, C., Zscheischler, J., Mahecha, M., Reichstein, M., 2015. Ranking drivers of global carbon and energy fluxes over land, in: *2015 IEEE International Geoscience and Remote Sensing Symposium (IGARSS)*, IEEE. pp. 4416–4419.
- Camps-Valls, G., Sejdinovic, D., Runge, J., Reichstein, M., 2019. A Perspective on Gaussian Processes for Earth Observation. *National Science Review* doi:<https://doi.org/10.1093/nsr/nwz028>.
- Camps-Valls, G., Verrelst, J., Muñoz-Marí, J., Laparra, V., Mateo-Jiménez, F., Gómez-Dans,

- J., 2016. A Survey on Gaussian Processes for Earth Observation Data Analysis. *IEEE Geoscience and Remote Sensing Magazine* 4.
- Chelton, D.B., Wentz, F.J., 2005. Global microwave satellite observations of sea surface temperature for numerical weather prediction and climate research. *Bulletin of the American Meteorological Society* 86, 1097–1116.
- Chen, J., Jönsson, P., Tamura, M., Gu, Z., Matsushita, B., Eklundh, L., 2004. A simple method for reconstructing a high-quality NDVI time-series data set based on the savitzky–golay filter. *Remote sensing of Environment* 91, 332–344.
- Chevrel, M., Courtois, M., Weill, G., 1981. The SPOT satellite remote sensing mission. *Photogrammetric Engineering and Remote Sensing* 47, 1163–1171.
- Cloude, S., 2010. *Polarisation: applications in remote sensing*. Oxford University Press.
- Dierckx, W., Sterckx, S., Benhadj, I., Livens, S., Duhoux, G., Van Achteren, T., Francois, M., Mellab, K., Saint, G., 2014. PROBA-V mission for global vegetation monitoring: standard products and image quality. *International Journal of Remote Sensing* 35, 2589–2614.
- Drusch, M., Del Bello, U., Carlier, S., Colin, O., Fernandez, V., Gascon, F., Hoersch, B., Isola, C., Laberinti, P., Martimort, P., et al., 2012. Sentinel-2: ESA’s optical high-resolution mission for GMES operational services. *Remote Sensing of Environment* 120, 25–36.
- Duchemin, B., Fieuzal, R., Rivera, M.A., Ezzahar, J., Jarlan, L., Rodriguez, J.C., Hagolle, O., Watts, C., 2015. Impact of sowing date on yield and water use efficiency of wheat analyzed through spatial modeling and FORMOSAT-2 images. *Remote Sensing* 7, 5951–5979.
- Dusseux, P., Corpetti, T., Hubert-Moy, L., Corgne, S., 2014. Combined use of multi-temporal optical and radar satellite images for grassland monitoring. *Remote Sensing* 6, 6163–6182.
- Errico, A., Angelino, C.V., Cicala, L., Persechino, G., Ferrara, C., Lega, M., Vallario, A., Parente, C., Masi, G., Gaetano, R., et al., 2015. Detection of environmental hazards through the feature-based fusion of optical and SAR data: A case study in southern Italy. *International Journal of Remote Sensing* 36, 3345–3367.

- Ferrazzoli, P., Paloscia, S., Pampaloni, P., Schiavon, G., Solimini, D., Coppo, P., 1992. Sensitivity to microwave measurements to vegetation biomass and soil moisture content: A case study. *IEEE Transactions on Geoscience and Remote Sensing* 30, 750–756.
- Fieuzal, R., Baup, F., Marais-Sicre, C., 2013. Monitoring wheat and rapeseed by using synchronous optical and radar satellite data - From temporal signatures to crop parameters estimation. *Advances in Remote Sensing* 2, 162.
- Ganguly, S., Nemani, R.R., Zhang, G., Hashimoto, H., Milesi, C., Michaelis, A., Wang, W., Votava, P., Samanta, A., Melton, F., et al., 2012. Generating global leaf area index from Landsat: Algorithm formulation and demonstration. *Remote Sensing of Environment* 122, 185–202.
- Gao, F., Anderson, M.C., Kustas, W.P., Wang, Y., 2012. Simple method for retrieving leaf area index from landsat using MODIS leaf area index products as reference. *Journal of Applied Remote Sensing* 6, 063554.
- Gao, F., Masek, J., Schwaller, M., Hall, F., 2006. On the blending of the Landsat and MODIS surface reflectance: Predicting daily landsat surface reflectance. *IEEE Transactions on Geoscience and Remote sensing* 44, 2207–2218.
- Gao, Q., Zribi, M., Escorihuela, M.J., Baghdadi, N., 2017. Synergetic use of Sentinel-1 and Sentinel-2 data for soil moisture mapping at 100 m resolution. *Sensors* 17, 1966.
- Golyandina, N., Osipov, E., 2007. The “caterpillar”-SSA method for analysis of time series with missing values. *Journal of Statistical planning and Inference* 137, 2642–2653.
- Gómez, V.P., Medina, V.D.B., Bengoa, J.L., García, D.A.N., 2018. Accuracy Assessment of a 122 Classes Land Cover Map Based on Sentinel-2, Landsat 8 and Deimos-1 Images and Ancillary Data, in: *IGARSS 2018-2018 IEEE International Geoscience and Remote Sensing Symposium*, IEEE. pp. 5453–5456.
- GPpy, 2012. GPpy: A gaussian process framework in python. <http://github.com/SheffieldML/GPy>.

- Haas, J., Ban, Y., 2017. Sentinel-1A SAR and sentinel-2A MSI data fusion for urban ecosystem service mapping. *Remote Sensing Applications: Society and Environment* 8, 41–53.
- Hagolle, O., Huc, M., Pascual, D.V., Dedieu, G., 2010. A multi-temporal method for cloud detection, applied to FORMOSAT-2, ven μ s, LANDSAT and SENTINEL-2 images. *Remote Sensing of Environment* 114, 1747–1755.
- He, W., Yokoya, N., 2018. Multi-Temporal Sentinel-1 and-2 Data Fusion for Optical Image Simulation. *ISPRS International Journal of Geo-Information* 7, 389.
- Houborg, R., McCabe, M., Gao, F., 2016. A Spatio-Temporal Enhancement Method for medium resolution LAI (STEM-LAI). *International Journal of Applied Earth Observation and Geoinformation* .
- Huete, A., Didan, K., Miura, T., Rodriguez, E.P., Gao, X., Ferreira, L.G., 2002. Overview of the radiometric and biophysical performance of the MODIS vegetation indices. *Remote sensing of environment* 83, 195–213.
- Johnson, J.E., Laparra, V., Camps-Valls, G., 2019. Accounting for input noise in gaussian process parameter retrieval. *IEEE Geoscience and Remote Sensing Letters* Advance online publication DOI:10.1109/LGRS.2019.2921476, 1–5.
- Jonckheere, I., Fleck, S., Nackaerts, K., Muys, B., Coppin, P., Weiss, M., Baret, F., 2004. Review of methods for in situ leaf area index determination Part I: Theories, sensors and hemispherical photography. *Agricultural and Forest Meteorology* 121, 19–35. doi:[10.1016/j.agrformet.2003.08.027](https://doi.org/10.1016/j.agrformet.2003.08.027).
- Jonsson, P., Eklundh, L., 2002. Seasonality extraction by function fitting to time-series of satellite sensor data. *IEEE transactions on Geoscience and Remote Sensing* 40, 1824–1832.
- Jönsson, P., Eklundh, L., 2004. TIMESAT-a program for analyzing time-series of satellite sensor data. *Computers & Geosciences* 30, 833–845.
- Joshi, N., Baumann, M., Ehammer, A., Fensholt, R., Grogan, K., Hostert, P., Jepsen, M.R., Kuemmerle, T., Meyfroidt, P., Mitchard, E.T., et al., 2016. A review of the application of

- optical and radar remote sensing data fusion to land use mapping and monitoring. *Remote Sensing* 8, 70.
- Journel, A., Huijbregts, C., 1978. *Mining Geostatistics*. Academic Press.
- Kandasamy, S., Baret, F., Verger, A., Neveux, P., Weiss, M., 2013. A comparison of methods for smoothing and gap filling time series of remote sensing observations-application to MODIS LAI products. *Biogeosciences* 10, 4055–4071.
- Kim, Y., Jackson, T., Bindlish, R., Hong, S., Jung, G., Lee, K., 2014. Retrieval of wheat growth parameters with radar vegetation indices. *parameters* 20, 23.
- Kim, Y., Jackson, T., Bindlish, R., Lee, H., Hong, S., 2012. Radar vegetation index for estimating the vegetation water content of rice and soybean. *IEEE Geoscience and Remote Sensing Letters* 9, 564–568.
- Kim, Y., van Zyl, J., 2001. Comparison of forest parameter estimation techniques using SAR data, in: *Geoscience and Remote Sensing Symposium, 2001. IGARSS'01. IEEE 2001 International*, IEEE. pp. 1395–1397.
- Kim, Y., van Zyl, J.J., 2009. A time-series approach to estimate soil moisture using polarimetric radar data. *IEEE Transactions on Geoscience and Remote Sensing* 47, 2519–2527.
- Lopez-Sanchez, J.M., Vicente-Guijalba, F., Ballester-Berman, J.D., Cloude, S.R., 2013. Estimating phenology of agricultural crops from space, in: *ESA Living Planet Symp.*, Edinburgh, UK.
- Malenovský, Z., Rott, H., Cihlar, J., Schaepman, M., García-Santos, G., Fernandes, R., Berger, M., 2012. Sentinels for science: Potential of Sentinel-1, -2, and -3 missions for scientific observations of ocean, cryosphere, and land. *Remote Sensing of Environment* 120, 91–101.
- Mandal, D., Kumar, V., Bhattacharya, A., Rao, Y.S., Siqueira, P., Bera, S., 2018. Sen4rice: A processing chain for differentiating early and late transplanted rice using time-series Sentinel-1 SAR data with Google Earth Engine. *IEEE Geoscience and Remote Sensing Letters* , 1–5.

- Mattia, F., Le Toan, T., Picard, G., Posa, F.I., D'Alessio, A., Notarnicola, C., Gatti, A.M., Rinaldi, M., Satalino, G., Pasquariello, G., 2003. Multitemporal C-band radar measurements on wheat fields. *IEEE Transactions on Geoscience and Remote Sensing* 41, 1551–1560.
- Piles, M., van der Schalie, R., Gruber, A., Muñoz-Marí, J., Camps-Valls, G., Mateo-Sanchis, A., Dorigo, W., de Jeu, R., 2018. Global Estimation of Soil Moisture Persistence with L and C-Band Microwave Sensors, in: *IGARSS 2018-2018 IEEE International Geoscience and Remote Sensing Symposium*, IEEE. pp. 8259–8262.
- Rasmussen, C.E., 2004. Gaussian processes in machine learning, in: *Advanced lectures on machine learning*. Springer, pp. 63–71.
- Rasmussen, C.E., Williams, C.K.I., 2006. *Gaussian Processes for Machine Learning*. The MIT Press, New York.
- Richardson, A.D., Keenan, T.F., Migliavacca, M., Ryu, Y., Sonnentag, O., Toomey, M., 2013. Climate change, phenology, and phenological control of vegetation feedbacks to the climate system. *Agricultural and Forest Meteorology* 169, 156–173.
- Satalino, G., Balenzano, A., Mattia, F., Davidson, M.W., 2014. C-band SAR data for mapping crops dominated by surface or volume scattering. *IEEE Geoscience and Remote Sensing Letters* 11, 384–388.
- Scarpa, G., Gargiulo, M., Mazza, A., Gaetano, R., 2018. A CNN-Based Fusion Method for Feature Extraction from Sentinel Data. *Remote Sensing* 10, 236.
- Schmitt, M., Hughes, L.H., Zhu, X.X., 2018. The SEN1-2 Dataset for Deep Learning in SAR-Optical Data Fusion. *arXiv preprint arXiv:1807.01569* .
- Szigarski, C., Jagdhuber, T., Baur, M., Thiel, C., Parrens, M., Wigneron, J.P., Piles, M., Entekhabi, D., 2018. Analysis of the Radar Vegetation Index and Potential Improvements. *Remote Sensing* 10, 1776.
- Torbick, N., Chowdhury, D., Salas, W., Qi, J., 2017. Monitoring rice agriculture across myanmar using time series sentinel-1 assisted by Landsat-8 and PALSAR-2. *Remote Sensing* 9, 119.

- Torres, R., Snoeij, P., Geudtner, D., Bibby, D., Davidson, M., Attema, E., Potin, P., Rommen, B., Floury, N., Brown, M., et al., 2012. GMES Sentinel-1 mission. *Remote Sensing of Environment* 120, 9–24.
- Tucker, C.J., 1979. Red and photographic infrared linear combinations for monitoring vegetation. *Remote sensing of Environment* 8, 127–150.
- Tupin, F., Roux, M., 2003. Detection of building outlines based on the fusion of SAR and optical features. *ISPRS Journal of Photogrammetry and Remote Sensing* 58, 71–82.
- Ulaby, F.T., Moore, R.K., Fung, A.K., 1981. Microwave remote sensing: active and passive, volume I: Microwave remote sensing fundamentals and radiometry. Artech House, Norwood, MA , 456–456.
- Veloso, A., Mermoz, S., Bouvet, A., Le Toan, T., Planells, M., Dejoux, J.F., Ceschia, E., 2017. Understanding the temporal behavior of crops using Sentinel-1 and Sentinel-2-like data for agricultural applications. *Remote Sensing of Environment* 199, 415–426.
- Verger, A., Baret, F., Weiss, M., 2011. A multisensor fusion approach to improve LAI time series. *Remote sensing of environment* 115, 2460–2470.
- Verger, A., Baret, F., Weiss, M., Kandasamy, S., Vermote, E., 2013. The CACAO method for smoothing, gap filling, and characterizing seasonal anomalies in satellite time series. *IEEE transactions on Geoscience and Remote Sensing* 51, 1963–1972.
- Verrelst, J., Alonso, L., Camps-Valls, G., Delegido, J., Moreno, J., 2012. Retrieval of vegetation biophysical parameters using Gaussian process techniques. *IEEE Transactions on Geoscience and Remote Sensing* 50, 1832–1843. Cited By 26.
- Verrelst, J., Alonso, L., Rivera Caicedo, J., Moreno, J., Camps-Valls, G., 2013a. Gaussian Process Retrieval of Chlorophyll Content From Imaging Spectroscopy Data. *IEEE Journal of Selected Topics in Applied Earth Observations and Remote Sensing* 6, 867–874.
- Verrelst, J., Malenovsky, Z., Van der Tol, C., Camps-Valls, G., Gastellu-Etchegorry, J.P., Lewis, P., North, P., Moreno, J., 2019. Quantifying vegetation biophysical variables from

- imaging spectroscopy data: a review on retrieval methods. *Surveys in Geophysics* 40, 589–629.
- Verrelst, J., Rivera, J., Veroustraete, F., Muñoz Marí, J., Clevers, J., Camps-Valls, G., Moreno, J., 2015. Experimental Sentinel-2 LAI estimation using parametric, non-parametric and physical retrieval methods - A comparison. *ISPRS Journal of Photogrammetry and Remote Sensing* 108, 260–272.
- Verrelst, J., Rivera, J.P., Moreno, J., Camps-Valls, G., 2013b. Gaussian processes uncertainty estimates in experimental Sentinel-2 LAI and leaf chlorophyll content retrieval. *ISPRS journal of photogrammetry and remote sensing* 86, 157–167.
- Wang, P., Gao, F., Masek, J.G., 2014. Operational data fusion framework for building frequent Landsat-like imagery. *IEEE Transactions on Geoscience and Remote Sensing* 52, 7353–7365.
- Wiseman, G., McNairn, H., Homayouni, S., Shang, J., 2014. RADARSAT-2 polarimetric SAR response to crop biomass for agricultural production monitoring. *IEEE J. Sel. Top. Appl. Earth Obs. Remote Sens* 7, 4461–4471.
- Xu, L., Zhang, H., Wang, C., Zhang, B., Liu, M., 2019. Crop Classification Based on Temporal Information Using Sentinel-1 SAR Time-Series Data. *Remote Sensing* 11, 53.
- Zhang, X., Friedl, M.A., Schaaf, C.B., Strahler, A.H., Hodges, J.C., Gao, F., Reed, B.C., Huete, A., 2003. Monitoring vegetation phenology using MODIS. *Remote sensing of environment* 84, 471–475.

Appendix A. Single- vs multi-output regression performance

Interpolation Method	R^2	ΣRes	RMSE
Fourier analysis: Offset + Harmonic analysis	0.5307	5.3803	0.9896
Polynomial curve fitting	0.8329	16.0240	2.3874
Double logistic curve	0.3127	8.8674	1.6912
Linear interpolation	0.3006	7.9026	1.3926
Nearest neighbor interpolation	0.9734	7.1444	1.3061
Next neighbor interpolation	0.0645	8.2933	1.4231
Previous neighbor interpolation	0.8433	7.6838	1.4651
Spline interpolation using not-a-knot end conditions	0.6620	5.0872	0.9798
Shape-preserving piecewise cubic interpolation	0.6963	7.3767	1.3220
Bagging trees	0.2120	10.1841	1.7216
Adaptive Regression Splines	0.7446	12.2503	1.9048
Boosting random trees	0.0014	8.9694	1.5074
Boosting trees	0.2859	8.2312	1.5876
k-nearest neighbours regression	0.1452	8.2350	1.5764
Gaussian Process Regression	0.9081	5.7816	0.9527
Neural networks	0.7481	7.5766	1.3005
Random forests	0.9734	7.1444	1.3061
Multi-Output Gaussian Process	0.9900	1.3035	0.2377

Table A.6: Performance of the set of 19 single-output regression methods applied to the LAI time series in Section 4.1.4 vs the proposed multi-output regression technique. In blue, the method providing the best score as a trade-off between R^2 and $RMSE$ for the two cases. A general description of the methods along with specific references to each of them can be found in Verrelst et al. (2019).

List of Figures

- Figure 1: Sketch of MOGP modelling based on the Linear Corregionalization Model (LCM). The time series of the two input parameters to be linked by MOGP, $\mathcal{D}_{P_{S1}}$ and $\mathcal{D}_{P_{S1}}$, are used to train the model. The trained MOGP model provides a prediction of P_{S1} and P_{S1} along with their uncertainty for each input time t .
- Figure 2: RGB image of the crop AOI in Castile and Leon region, Northwest Iberian peninsula, from Sentinel2 capture of 2017, April 12th. The yellow dotted rectangle delimits the subset analyzed in Section 4.2.2.
- Figure 3: Histograms of Pearson’s correlation coefficient ρ_t through time calculated per-pixel using all possible pairs of S2(NDVI,LAI) and S1(VV,VH,VH/VV,RVI) parameter time series over the AOI.
- Figure 4: Spatial distribution of temporal correlation ρ_t between LAI and SAR vegetation descriptor time series - VV(a), VH(b), RVI (c) - and map of descriptor with the highest ρ_t (d) over the AOI.
- Figure 5: Statistical behavior (mean value and standard deviation) of LAI(a) and ascending(red) and descending(blue) RVI(b) time series over a selected parcel from November 2015 to end of October 2018. Inteval A in (b) indicates soil contribution to RVI impairing SAR co-/cross-polar balance between the two geometries. The main phenological stages of a crop are qualitatively sketch along the second season in (a), as qualitative reference.
- Figure 6: MOGP predictions (circles) of LAI (a) and RVI (b) on the union of S1 and S2 acquisition dates provided by the MOGP model trained on input time series (asterisks). The uncertainty of $\pm 2\sigma$ is represented by the boundary shade (grey) at any estimate. In (a), interval B indicates the realistic end of tillering dynamics obtained by fusing RVI information; interval C the higher uncertainty of LAI retrieval due to local differences between training samples of LAI (C) and of RVI (E) over the same period. In (b), intervals D and F indicate local inconsistencies between ascending and descending RVI samples likely due to anisotropic soil contributions.
- Figure 7: Assessment of standard GPR(a) and MOGP(b) predictions (blue circles) for data gap filling on S2 cloud-free captures (magenta) eliminated from training informa-

tion (red asterisks) and here used as reference. The $\pm 2\sigma$ prediction uncertainty is represented by the boundary shade (grey) at any estimate. Intervals S in (a) and (b) evince the more realistic dynamics retrieved by MOGP during the stemming stages.

Figure 8: Spatial distribution over the AOI and histograms over crop areas of ℓ parameter for LFGP and HFGP (a,b and c in upper panel), and of b_{12}^{LF} and b_{12}^{HF} (d,e,f in lower panel).

Figure 9: Spatial distribution of the ratios between high- (a) and low-frequency (b) coefficients in (10).

Figure 10: LAI maps from S2 image (reference), MOGP and standard GP, error histograms and scatter plots for two dates: 2016/2/17 and 2016/04/27 (90 days gap from 2016/1/18 to 2016/4/17).

Figure 11: LAI maps from S2 image (reference), MOGP and standard GP, error histograms and scatter plots for 2017/4/12 (50 days gap from 2017/3/13 to 2017/5/2).

Figure 12: Comparison of LAI maps from S2 image (reference), MOGP and standard GP over a subset of AOI (yellow rectangle in Figure 2) corresponding to 4/2, 4/12 and 4/22 within the 50 days gap from 2017/3/13 to 2017/5/2. LAI evolution provided by GPR is more unlikely than MOGP's results.